ANALYSIS AND UNDERSTANDING OF HEAT TREATMENT OF L-PBF TITANIUM PRODUCTS

Philip Simões Carvalho

Thesis to obtain the Master of Science Degree in

Mechanical Engineering

Supervisors: Prof. Eurico Gonçalves Assunção
Prof. Inês da Fonseca Pestana Ascenso Pires

Examination Committee

Chairperson: Prof. Rui Manuel dos Santos Oliveira Baptista
Supervisor: Prof. Eurico Gonçalves Assunção
Members of the Committee: Prof. Ivo Manuel Ferreira de Bragança
Eng. Seán McConnell

September 2021

Acknowledgments

Firstly I would like to thank my supervisors, Prof. Eurico Assunção and Prof. Inês Pires, for all the guidance provided throughout the duration of my thesis and the opportunity given to me to work with Irish Manufacturing research.

I would also like to thank everyone at IMR and especially Sean McConnell and Beatriz Ropio for their kindness and help during my short time in Ireland and the remainder of my thesis.

I would also like to thank Professors Carlos Silva and Ivo Bragança for all of the time spent helping and guiding me through the experimental procedures.

I would like to extend my personal thanks to all of my friends who were with me and helped me through this part of my life.

Lastly, I'd like to thank my family from the bottom of my heart for their incessant love and support. To my Mom, my Dad, my Sister and all of my Grandparents.

Resumo

O mundo da impressão 3D tem aberto muitas portas em relação a produzir partes feitas em metal devido às suas geometrias complexas e os diferentes materiais que podem ser utilizados para as produzir. No entanto, embora seja muito útil, a impressão através de L-PBF continua a produzir peças com defeitos severos como descontinuidades na zona de derretimento e material vaporizado preso no interior da peça. Estes defeitos têm graves consequências nas propriedades mecânicas das peças. Para resolver estes problemas, existem vários tipos de pós-processamentos que podem ser utilizados nas peças produzidas, nomeadamente tratamentos térmicos.

Este trabalho foi desenvolvido com o objetivo de determinar como os parâmetros dos tratamentos térmicos afetam as propriedades mecânicas finais de peças de titânio produzidas por L-PBF. Um total de 86 provetes foram produzidos, dos quais 81 foram submetidos a tratamentos térmicos com várias combinações diferentes de tempos de cozedura, temperaturas de cozedura e taxas de arrefecimento. O DOE foi criado com o auxílio de um software estatístico. A seguir, algumas propriedades mecânicas foram obtidas através de ensaios de tração e de microdureza. Por último, os parâmetros otimizados foram obtidos através de uma análise feita utilizando o mesmo software estatístico.

Concluiu-se que replicar os mesmos resultados numa impressão L-PBF é complicado quando não há um controlo sobre todas as variáveis, como os parâmetros de impressão ou a qualidade da matéria-prima. Apenas um conjunto de parâmetros pode ser utilizado para cada impressão diferente pois a mais ligeira mudança, como mudar a orientação dos componentes, pode tornar os parâmetros de impressão inválidos. Quanto mais alta for a temperatura de cozimento, maior será a dureza.

Palavras-chave: Titânio, L-PBF, Propriedades Mecânicas, Tratamentos Térmicos

Abstract

3D printing has brought on an endless number of possibilities when it comes to producing parts made of metal due to the complex geometries and the wide variety of different materials that can be used to produce them. However, while very useful, printing through Laser Powder Bed Fusion still results in the production of parts with many crippling flaws like melt pool discontinuities and entrapped vaporized material that have a significant impact in their mechanical properties. To solve these issues, a number of different post-treatment processes can be applied to the produced parts, namely heat treatments.

This work strived to determine how regular heat treating parameters affect the final mechanical properties of titanium alloy L-PBF produced parts. A total of 86 testing coupons were produced, 81 of which were submitted to heat treatments with several different combinations of sitting temperatures, sitting times and cooling rates. The Design of Experiments was created using a statistical software. After, some mechanical properties of the 84 coupons were obtained through tensile and hardness testing. Lastly, the optimal parameters for enhancing the desired properties were obtained through an analysis performed using the same statistical program.

It was concluded that replicating the same results in an L-PBF print is complicated when there isn't a tight control over all variables like printing parameters or the quality of the powder. Only one set of parameters can be used for each print type as even the slightest difference, like changing the orientation of the components, can render the parameters non-optimal. The higher the resting temperature in the heat treatments is, the higher the hardness.

Keywords: Titanium, L-PBF, Mechanical Properties, Heat Treatment

Contents

Acknowledgments . . . iii

Resumo . . . v

Abstract . . . vii

List of Tables . . . xi

List of Figures . . . xiii

Nomenclature . . . xvii

Glossary . . . 1

1 Introduction 1

1.1 Motivation . . . 1

1.2 Topic Overview . . . 1

1.3 Objectives . . . 2

1.4 Dissertation Outline . . . 2

2 Literature Review 3

2.1 Laser - Powder Bed Fusion . . . 3

2.1.1 Introduction . . . 3

2.1.2 How it Works . . . 4

2.1.3 Process Parameters and Details . . . 5

2.1.4 Defect Creation Mechanisms . . . 9

2.2 Titanium and its Alloys in L-PBF . . . 12

2.2.1 Microstructure . . . 12

2.2.2 The Ti-6Al-4V Alloy . . . 13

2.2.3 Typical Defects . . . 22

3 Experimental Approach 25

3.1 Overview of the Experimental Approach . . . 25

3.2 Material . . . 26

3.3 Printing the Coupons . . . 26

3.4 Design of Experiments . . . 27

3.5 Equipment . . . 29

3.5.1 Coupon Design . . . 29

3.5.2 L-PBF Printing System 29
3.5.3 Heat Treatments 29
3.5.4 Polishing and Grinding 30
3.5.5 Tensile Testing 30
3.5.6 Microhardness Testing 31

4 Results and Discussion **33**
4.1 As-Built Coupons 33
4.2 Heat Treated Coupons 35
4.2.1 Sitting Temperature - 800 °C 35
4.2.2 Sitting Temperature - 950 °C 36
4.2.3 Sitting Temperature - 1100 °C 38
4.2.4 Overall Analysis 39

5 Conclusions **45**
5.1 Future Work 46

Bibliography **47**

A Process Parameters **53**
A.1 Coupon Heat Treatment Parameters 53
A.2 Previous Work's Tensile Testing Results 55

B Mechanical Testing Results **56**
B.1 Stress vs Strain Plots 56
B.2 Hardness Measurements 65

List of Tables

2.1 Selected microstructural features and effect on properties of titanium alloys. [27] 14

3.1 Composition of the powder used to produce the testing coupons according to the manufacturer. 27

3.2 Size distribution of the powder according to the manufacturer. 27

3.3 List of the main printing parameters. 27

3.4 Design of Experiments. 28

4.1 Results obtained from tensile testing done to the non heat treated coupons. 34

4.2 Tensile testing results for the coupons heat treated at 800 °C. 36

4.3 Tensile testing results for the coupons heat treated at 950 °C. 37

4.4 Tensile testing results for the coupons heat treated at 1100 °C. 38

4.5 Tensile testing results of the heat treated coupons. 40

4.6 Surface microhardness [HV] values obtained for the heat treated components. 42

4.7 Surface microhardness [HV] values obtained for the as-built parts. 42

4.8 Average microhardness [HV] values for coupons treated with a certain parameter. 42

5.1 Heat treating parameters that yielded the best results. 46

A.1 Detailed list of the different combinations of parameters used to produce the testing coupons. 54

A.2 Results from the tensile testing performed in the previous work. 55

B.1 Hardness measurement results, shown in [HV]. 65

List of Figures

2.1 General overview of an L-PBF machine. 4

2.2 Representation of various SLM parameters. [2] 7

2.3 Examples of different scanning strategies: (a) 45°Alternating (b) 90°Alternating (c) Schematic of Chessboard Scanning (d) Chessboard Scanning with Adjacent Chessboard block Scanned in 45°rotated direction. (e) Chessboard Scanning with Adjacent Chessboard block Scanned in 90°rotated direction. [8] 8

2.4 Cross section of a Ti-6Al-4V sample showing a large number of near-spherical defects caused by material vaporization. [18] 10

2.5 Schematic representation of the forming of pits through the removal of welded particles by the re-coating blade. [18] 10

2.6 Defects caused by mass transfer showing both the welded particles and the pits where removed particles were. [18] 11

2.7 Melt pool discontinuity in a Ti-6Al-4V sample. [18] 11

2.8 Chemical composition of Ti-6Al-4V. [28] 14

2.9 Phase diagram of Ti-6Al-4V. [29] 15

2.10 L-PBF produced Ti-6Al-4V a) Columnar prior-β grains filled α' martensite with 30 μm layer thickness b) ultrafine lamellar $\alpha+\beta$ structure with 60 μm layer thickness c) acicular α' with minor $\alpha + \beta$ lamellae using a layer thickness of 90 μm, d) detail of a). [21] 15

2.11 CCT diagram of Ti-6Al-4V. [21] 16

2.12 Top (a) and side (b) view of untreated Ti-6Al-4V produced by L-PBF. The chessboard pattern is due to the scan pattern used to produce this part. Columnar prior-β grains can also be seen in the side view. [30] 17

2.13 Microstructure of Ti-6Al-4V produced by PBF after heat treating at different temperatures for 2 h, followed by furnace cooling. (a) 780 °C (b) 843 °C (c) 1015 °C. Lighter zones are β phase, the dark phase is the α phase. [30] 18

2.14 Stereological parameters of lamellar microstructure: D – primary β-phase grain size, d – size of the colony of parallel α-lamellae, t – thickness of α-lamellae. [21] 19

2.15 Hardness evolution of the Ti-6Al-4V microstructure as a function of the tempering temperature after a solution treatment at 1050 °C during 1 h WQ, for both air and furnace cooling. [26] 21

2.16 Fatigue performances of SLMed, HIPed, HT-920 and HT-850-550 Ti-6Al-4V specimens. [39] 22

3.1 Flowchart of the experimental approach. 26
3.2 The print layout of the testing coupons viewed in the software. 28
3.3 As-built coupon still attached to the print bed with supports visible. 28
3.4 The Renishaw RenAM 500M. 29
3.5 The Struers LaboPol-30 used to polish the samples. 30
3.6 The Static Axial Clip-On Instron Extensometer clipped onto a coupon. The 3D printed part can be seen on the extensometer in orange. 30
3.7 Left Image: The Struers Duramin used to perform the microhardness tests. Right Image: The Instron 4507 used to run the tensile tests. 31

4.1 Fracture surface of coupon P5. 34
4.2 Graphical representation of the UTS and the elongation according to the applied heat treatment, more specifically, at the sitting temperature of 800 °C. 36
4.3 Graphical representation of the UTS and the elongation according to the applied heat treatment, more specifically, at the sitting temperature of 950 °C. The vertical red lines indicate the coupons that fractured prior to reaching the elastic region. 37
4.4 Fracture surface of coupon 15 with a zoomed in area showing a brown spot, which is unexpected in this material. 37
4.5 Graphical representation of the UTS and the elongation according to the applied heat treatment, more specifically, at the sitting temperature of 1100 °C. The vertical red lines indicate the coupons that fractured prior to reaching the elastic region. 39
4.6 Fracture surface of a coupon treated at 1100°C. 39
4.7 Graphical representation of the UTS and the elongation according to the applied heat treatment, more specifically, the sitting temperature. The vertical red lines indicate the coupons that fractured prior to reaching the elastic region. 40
4.8 Microstructure of an SLMed sample after being heat treated at 850°C for 2h and being water quenched. [35] 41
4.9 Graphical representation of the hardness and the elongation according to the applied heat treatment, more specifically, the sitting temperature. The vertical red lines indicate the coupons that fractured prior to reaching the elastic region. 43

B.1 Stress vs Strain plot for sample number P4. 56
B.2 Stress vs Strain plot for sample number P5. 57
B.3 Stress vs Strain plot for sample number 1. 57
B.4 Stress vs Strain plot for sample number 3. 58
B.5 Stress vs Strain plot for sample number 4. 58
B.6 Stress vs Strain plot for sample number 6. 59
B.7 Stress vs Strain plot for sample number 10. 59

B.8 Stress vs Strain plot for sample number 12. 60
B.9 Stress vs Strain plot for sample number 18. 60
B.10 Stress vs Strain plot for sample number 19. 61
B.11 Stress vs Strain plot for sample number 20. 61
B.12 Stress vs Strain plot for sample number 21. 62
B.13 Stress vs Strain plot for sample number 24. 62
B.14 Stress vs Strain plot for sample number 27. 63
B.15 Stress vs Strain plot for sample number 28. 63
B.16 Stress vs Strain plot for sample number 32. 64

Nomenclature

AC	Air Cooling
DOE	Design of Experiments
FC	Furnace Cooling
HIP	Hot Isostatic Pressing
L-PBF	Laser Powder Bed Fusion
OQ	Oil Quenching
SEM	Scanning Electron Microscope
UTS	Ultimate Tensile Strength
WQ	Water Quenching
YS	Yield Strength

Chapter 1

Introduction

1.1 Motivation

Ensuring the best possible results when producing titanium alloy parts through Laser Powder Bed Fusion is of utmost importance as these parts will be used in applications where mechanical failure is not an option. It is known that putting these parts through certain extreme temperature variations can alter their mechanical properties either through the elimination of defects or through the change in microstructure. Depending on how they're used, they can improve or deprecate the heat treated component's mechanical performance.

Understanding how these heat treatments affect these parts will provide the knowledge needed to efficiently treat them after production in order to obtain the desired mechanical properties.

1.2 Topic Overview

Additive manufacturing consists in producing parts layer by layer. As opposed to traditional ways of manufacturing, it usually allows for more complex geometries with less steps at the cost of higher prices and longer manufacturing times. It can use a wide variety of materials like metals, plastics or resins that, in turn, can come in many forms like powder or wire.

While useful, there is still a long way to go regarding the production of parts that are ready to be used as-built. The high production cost and the long manufacturing times make it so only the industries that can benefit the most from it can use it, like the aerospace and the medical industries. With their tight tolerances and requirement for complex and custom parts, the need to improve the overall quality is clear. This can be done through two approaches: improving and perfecting the build parameters of the part or subjecting the part to post-processing like surface finishing or heat treating.

There are already a wide variety of known heat treating methods that yield specific results in specific materials. However, these are more established for parts produced through traditional manufacturing. Parts produced through additive manufacturing acquire specific defects that require different types heat treatments. While some studies have been done in this field, it is still open to more research.

1.3 Objectives

The objective of this dissertation is to understand how the different heat treating parameters (sitting time, sitting temperature and cooling rate) affect the mechanical properties of L-PBF produced Ti-6Al-4V parts.

1.4 Dissertation Outline

This dissertation is divided into 5 main chapters: Laser Powder Bed Fusion, Titanium and its Alloys, Experimental Approach, Results & Discussion and Conclusion.

The 1st chapter introduces the thesis. The 2nd chapter focuses on all the ins and outs of L-PBF including its uses, how it works and analysis of all the parameters that affect the production as well as seeking to provide a general overview of the material used, titanium alloys and specifically Ti6Al4V. It encompasses a description of its uses, microstructure, properties and response to heat treatments. On chapter 3, the experimental procedure is described by enunciating all the machines and processes used as well as the DOE. Lastly, chapters 4 and 5 present the obtained results and their discussion, and the reached conclusions, respectively.

Chapter 2

Literature Review

2.1 Laser - Powder Bed Fusion

2.1.1 Introduction

TWI defines 3D printing, also known as additive manufacturing, as a ”method of creating a three dimensional object layer-by-layer using a computer created design”. It is an additive process whereby layers of material are built up to create a 3D part. This is the opposite of subtractive manufacturing processes, where a final design is cut from a larger block of material. As a result, 3D printing creates less material wastage.

3D printing first started in 1981 when Dr. Hideo Kodama filed a patent for a system that cured resin with a laser beam. 7 years later, in 1988, the first process that involved melting material was invented. Carl Deckard created the first selective laser sintering machine but it was only able to create simple chunks of plastic at the time. The first uses of metal in additive manufacturing came later in the 1990s and 2000s from research in universities, national labs and industrial R&D Labs which resulted in technical collaborations.

Currently there are 3 broad types of additive manufacturing:

- **Sintering** - technology where powdered material is heated, but not to the point of melting, to create high resolution items.
- **Melting** - technology where powdered material is melted. Heat sources include lasers, electric arcs and electron beams.
- **Stereolithography** - utilizes photopolymerization to create parts through a light source that interacts with the material in a selective manner to cure and solidify a cross section of an object in thin layers.

According to the ISO/ASTM 52900 standard, 3D printing can be further categorized into 7 groups:

Binder Jetting, Direct Energy Deposition, Material Extrusion, Material Jetting, Powder Bed Fusion, Sheet Lamination and VAT Polymerization. [1]

2.1.2 How it Works

This process consists on creating parts in layers by melting the material in the shape of each cross-section. This is done by a specialized machine that deposits layers of the used material one by one. The material used can be metallic, ceramic or even composite.

To start off, a CAD file of the product must be created, saved as a Stereolithography file (.STL) and then it is processed through a specific software, like QuantAM or Magics, to prepare it for the actual building process. This software creates slice data for laser scanning of the individual layers and generates supports for any overhanging features.

Now, the files are ready to be used. The building process starts with laying a thin layer of metal powder on a substrate plate in a building chamber. After the powder is laid, a high energy density laser is used to melt and fuse selected areas according to the processed data. Once the laser scanning is completed, the building platform is lowered, a next layer of powder is deposited on top and the laser scans a new layer. The process is then repeated for successive layers of powder until the required components are completely built. Process parameters, such as laser power, scanning speed, hatch spacing and layer thickness are adjusted such that a single melt vector can fuse completely with the neighbouring melt vectors and the preceding layer. Once the laser scanning process is completed, loose powders are removed from the building chamber and the component can be separated from the substrate plate manually or by electrical discharge machining (EDM). [2]

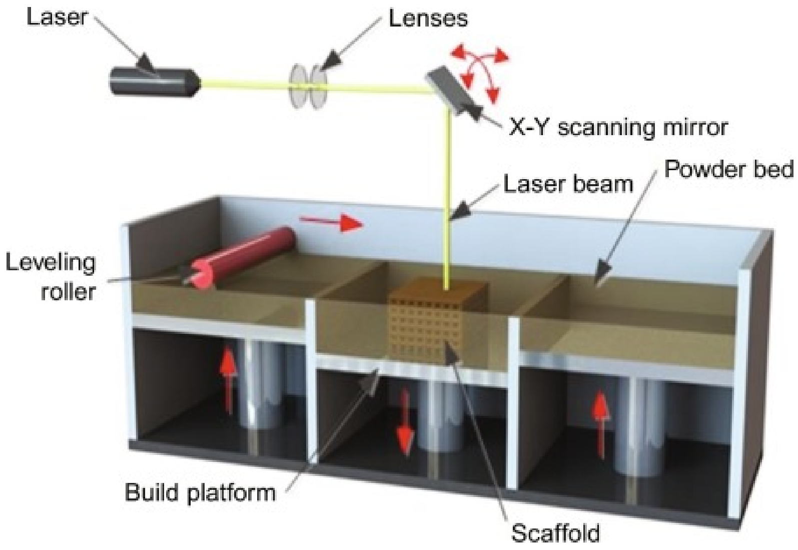

Figure 2.1: General overview of an L-PBF machine.

2.1.3 Process Parameters and Details

Build Volume

The build volume is the space where the building process takes place. It can be cylindrical or box shaped, although the latter is more common. It can reach sizes up to 1000x1000x500 mm (eg. ADIRA AddCreator from ADIRA) although machines with a build volume of up to 0.125 m^3 are more common as they usually take less time to produce (due to their smaller space) and use less material to work.

The build atmosphere is usually filled with an inert gas, such as Nitrogen or Argon, to remove reactive gases, such as Oxygen, and stop them from affecting the metal while it's being produced. Using different inert gases may also produce slight differences in the mechanical properties of the work piece. [3]

Laser Type

One of the most important parts of the process is how the machine melts the powder. This is done with lasers. Depending on the machine, these can one or more lasers working simultaneously. The whole laser system usually includes the laser source, focus lenses and a scanning mirror that directs the laser. The scanning mirror can be made of a number of materials depending on the nature of the laser. Lasers are usually classified by their gain medium. There are 3 main types of laser used in L-PBF: CO_2 lasers, Nd:YAG lasers and Yb-fiber lasers. Lasers have some parameters, controllable or not, that have great effects on the melting process.

The **operating wavelength** is the most important parameter due to the way that different materials react to different wavelengths. This affects the material's absorptivity. It is desirable to maximize absorptivity to ensure greater efficiency. Nd:YAG and Yb-fiber lasers have an operating wavelength of 1064 nm whereas CO_2 lasers have a 10.6 μm operating wavelength. Metal powders have its absorptivity inversely proportional to the operating wavelength. As such, Nd:YAG and Yb-fiber lasers are preferable when working with metallic powders. The operating wavelength is also related to focusability, which determines the ultimate manufacturing resolution.

The laser's **intensity** is defined as the power per unit of area that its able to deliver to the powder. It must be able to deliver enough power to cause the material to melt. Depending on the material's fusion point, thermal diffusivity and reflectivity, the laser will have to deliver more or less power. When interacting with metals that possess high thermal diffusivity and reflectivity more intensity is required to overcome the slow temperature increase. Build rate can be increased with intensity but at the cost of it being more prone to defect creation. Since the intensity is inversely proportional to the square of the laser wavelength lasers with higher wavelength, like the Yb-fiber, are able to deliver higher quality beams at the same power level when compared to lasers with lower wavelengths, like CO_2 lasers.

A laser's **operation mode** can be classified into pulsed mode or continuous mode. Continuous mode delivers constant power independent of time whereas pulsed mode emits peaks of power for a short pulse alternated with absence of power delivery. The three laser types used in L-PBF can work in both modes. Pulsed mode has some advantages: the high peak power can instantaneously increase the the temperature of the material to the melting point avoiding most thermal diffusivity. On the other hand, continuous mode would allow a lot of energy to be dissipated to the surroundings.

The last parameter worth mentioning is the **beam quality** which refers to its spatial domain and quantifies its manufacturing precision. This can be defined using the 'Beam Parameter Product' (BPP). This is calculated by taking the product of the beam radius (measured at the waist) and of the half angle of the beam divergence (measured in the far field) originating units of mm.mrad. This factor depends on some different parameters among which is the operating wavelength. It determines the lower limit of the BPP which is $\frac{\lambda}{\pi}$, also known as the diffraction-limit. The M^2 factor (beam quality factor) is another way of expressing the beam quality regardless of wavelength. It is calculated by dividing the BPP by $\frac{\lambda}{\pi}$ which is 1 when the laser beam is in perfect Gaussian shape. Simply put, the lasers that can reach beam quality factors close to 1 are the Yb:YAG and the CO_2 lasers due to the way they produce the laser.

In the end, Yb-fiber lasers are preferred due to their shorter wavelength, which allows for better absorptivity when working with metal powders, and their higher efficiency when compared to CO_2 lasers. [4]

Scanning Speed

The scanning speed is the speed at which the heat source travels through the powder bed. When defining it it in a process, other factors must be taken into account such as laser power, hatch spacing and layer thickness to ensure the desired result. The faster it is, the less heat penetration there will be and the less melted material resulting in defects like lack of continuity and fusion, and balling [4]. On the other hand, lower scanning speed extends the time that the laser interacts with the material ensuring greater melting capabilities and heat transfer into previously scanned layers reducing porosity in lower layers. [5] They can range from a few hundred mm/s to a few m/s.

Hatch Spacing

Hatch spacing relates to the distance between the centerlines of 2 consecutive passings of the laser in the powder bed. It should be small enough that the melt pools of each passing overlap enough to ensure continuity and avoid unwanted defects.

Layer Thickness

The amount of powder that is laid out each layer has great influence in the final properties of the work piece. This is also the distance that the base plate is lowered each time. Better results are usually obtained with thinner layers as there's less material to melt at a time. Using thicker layers increases the risk of there being unmelted particles, lack of fusion and air-traps which is in-line with the observed decrease in density. It also decreases microhardness, Young's modulus and UTS. [6] Typical layer thicknesses are in the 20 - 200 μm range. [7]

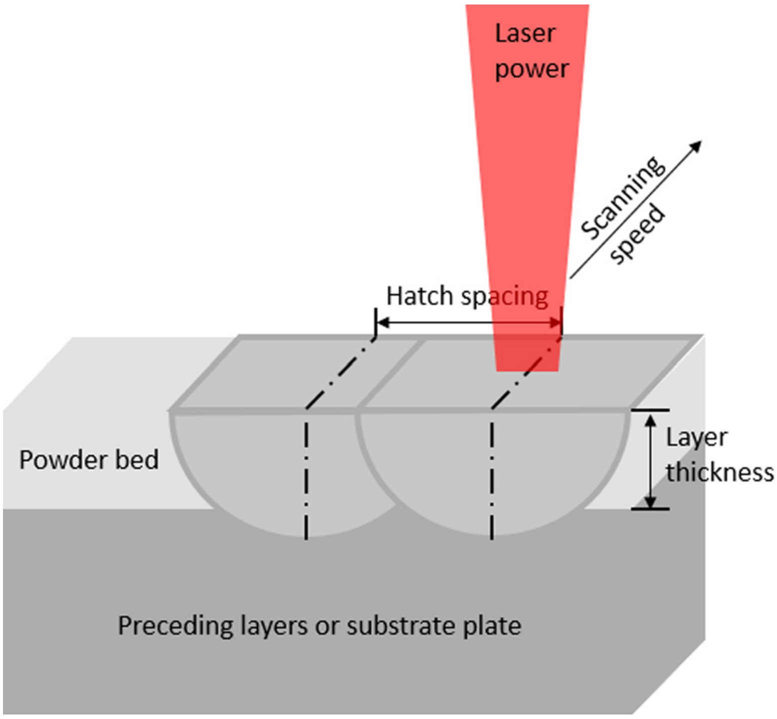

Figure 2.2: Representation of various SLM parameters. [2]

Scanning Strategies

The scanning strategy is the path that the laser takes to melt the material. These can be very varied and change from layer to layer. In figure 2.3, various different scanning strategies are shown. Choosing the correct scanning strategy is of utmost importance as it affects mechanical properties, porosity and residual stresses. The microstructure doesn't change as it remains fully martensitic with martensitic α' laths growing inside columnar prior β grains. Another factor that influences the end result is the scan vector length as the longer it is, the bigger the cooling rate of the reheated melted material is. [8]

Metal Powder

The metal powder is the material used to produce the final parts. There are a number of characteristics that are important to be kept in check to ensure smooth flowability and high packing density. Depending on the atomisation process used to produce the powder, it can take many shapes but for PBF use, the most desirable one is spherical. This is because they conform towards unity and can gradually enhance both its powder packing density and rheology performance. Thus, qualified feedstocks consist of mostly spherical particles with few irregularly shaped grains. Another important metric is PSD (particle size distribution) and it quantifies the size distribution of the particles in terms of volume composition. Changes in particle size originate mainly from recycling. Most commercial powders follow a Normal distribution with other common distributions being bi- and tri-modal (exhibit 2 or 3 peaks). Using coarser grain sizes leads to weaker mechanical strength due to the interstices left unfilled which may act like crack initiators. Finer grain sizes lead to lower ductility due to the increase in absorptivity and subsequent generation of a finer microstructure. Bi-modal distributions, when compared to normal, have been recorded to produce parts with higher UTS and lower yield strength. Some powders can be highly reactive to external elements triggering oxidation reactions. This can cause instability in the melt pool causing droplets, known as the balling effect. [9] The spherical metal powder typically has a diameter in the 15-70 μm range. [10] The powder atomization method (e.g. gas or plasma) can have a final influence in the mechanical properties of the print even if the particle distribution is the same. [11]

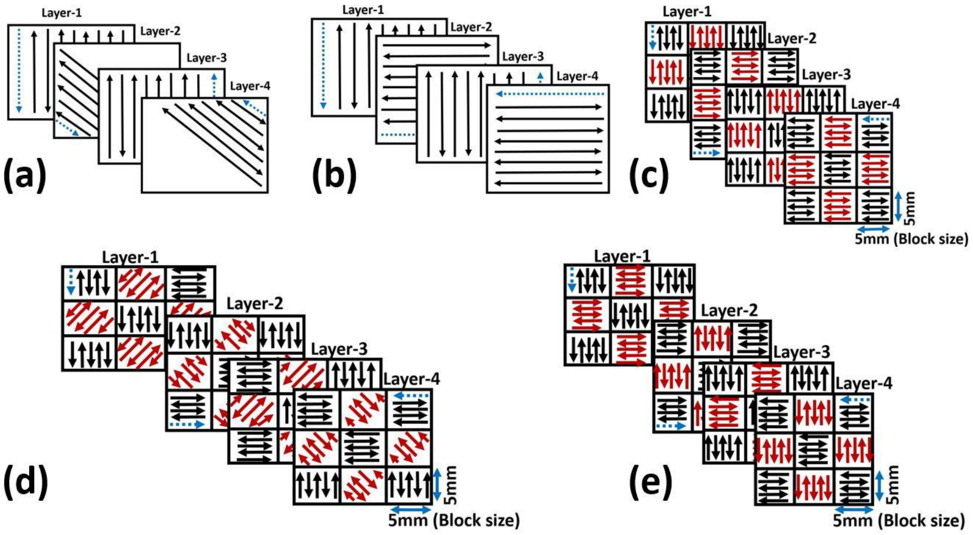

Figure 2.3: Examples of different scanning strategies: (a) 45°Alternating (b) 90°Alternating (c) Schematic of Chessboard Scanning (d) Chessboard Scanning with Adjacent Chessboard block Scanned in 45°rotated direction. (e) Chessboard Scanning with Adjacent Chessboard block Scanned in 90°rotated direction. [8]

Build Orientation

This is the way the samples are laid out on the bed when building. This can affect all aspects in the produced parts including microstructure, surface finishing, fracture mechanisms and mechanical properties. For example, there can be a reduction of about 10% to 13% in the UTS and yield strength when printing vertically as opposed to horizontally [12, 13]. The same part built in different orientations will have an anisotropic structure. Pieces built along their length direction experience smaller cooling rates than those that aren't. It is recommended to build the parts along the length direction as that will ensure better mechanical performance. [14] The build orientation can also play a role in avoiding thermal deformations that may take place. For example, thin pieces should be built on their side or upright to avoid curling due to thermal stresses that are very common in this type of processes. [13]

Volumetric Energy Density

Energy density is a key parameter when working with L-PBF as it relates a group of other very important parameters. It is denoted by E_V (in $J.mm^{-3}$) and defined as:

$$E_V = \frac{P}{vth}$$

where P is the laser power (in $J.s^{-1}$), v is the laser scanning velocity (in $mm.s^{-1}$), t is the layer thickness (in mm) and h is the hatch distance (in mm). It's worth noting that the scanning velocity is sometimes not directly defined but calculated as quotient of the melt point distance (distance between centers) and the exposure time in each point. This metric provides a method of controlling the microstructure of Ti-6Al-4V specimens and therefore, optimize the microhardness value. Low E_V values result in a relatively fine, weakly textured microstructure, with high density and with hardness values greater than those achieved by traditional processing methods. It also influences porosity levels, material density and the internal stresses that induce random texture and nucleation of equiaxed prior β-grain size. [15] For example, if the energy density is below 40 $J.mm^{-3}$, porosity due to unmelted powder is unavoidable regardless of other parameters. Likewise, if the energy density is too high, porosity will form due to overmelting. [16]

Support Structures

These serve a number of purposes among which are fixation to the build plate, fixation in the powder bed, heat dissipation, support for horizontally-oriented surfaces and extra rigidity to help avoid deformation through residual or thermal stresses. These usually have a lattice structure and are later removed when finishing the part. [17]

2.1.4 Defect Creation Mechanisms

This manufacturing process is very prone to inducing a wide variety of defects. These can be caused due to poorly chosen printing parameters or defective raw material which isn't uncommon due to the demanding specifications at which it is produced. Below are described the main defect creation mechanisms found in L-PBF printed parts.

Material Vaporization

This phenomenon occurs when there is an excess of energy output. It causes the vaporization of the constituents with the lowest melting points in the melt pool. The gas bubbles are formed far beneath the surface at the bottom of the melt pool. The high solidification rate of the melt pool and the fact that the thermal energy is conducted downwards, causing a temperature gradient, results in the entrapment of the bubbles that were formed in at the bottom. The result can be seen in fig. 2.4.

These defects are stochastically distributed throughout the produced pieces and are created in the prior layers of the material while depositing the new one. This means that porosity originated through this mechanism will not appear as surface defects. [18]

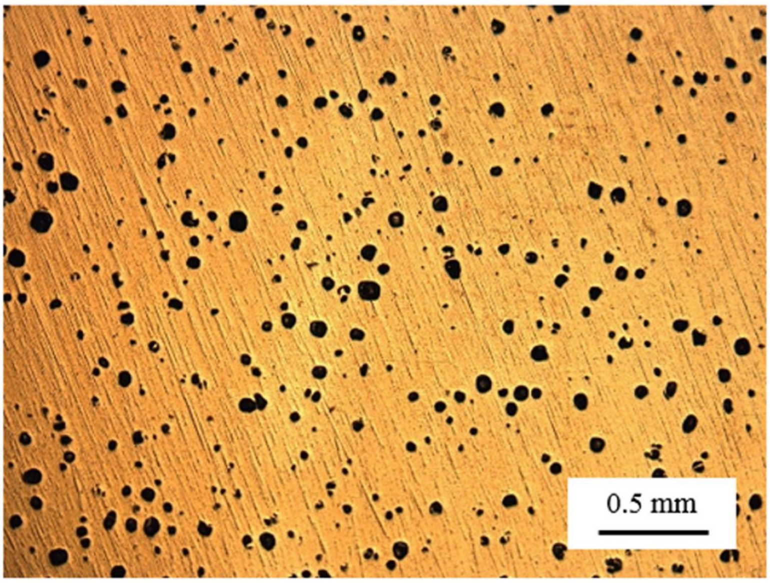

Figure 2.4: Cross section of a Ti-6Al-4V sample showing a large number of near-spherical defects caused by material vaporization. [18]

Mass Transfer Phenomenon

When there is excessive laser irradiation, an intense thermal energy is generated which evaporates molten material on the surface. The melt pool is subject to recoil pressure from the evolving vapor, which ejects molten materials. This means that the thermal energy not only causes reactions on a microscopic level, but also macroscopically.

When the molten material is ejected, it rapidly solidifies and, upon landing somewhere else in the powder bed, welds the powder around it. Small particles remain on the surface during spreading of the next layer. Particles larger than the layer thickness are removed by the re-coating blade leaving behind pits. This phenomenon is represented in fig. 2.5 and fig. 2.6. Most pits are filled when the next layer is added, however large pits with limited melt pool overlap might stay behind as defects.

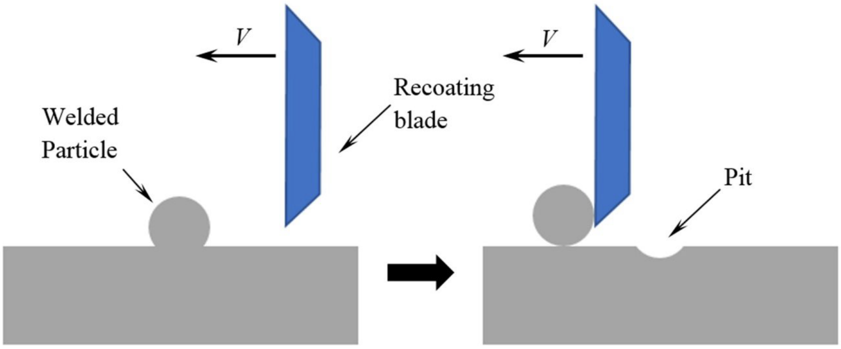

Figure 2.5: Schematic representation of the forming of pits through the removal of welded particles by the re-coating blade. [18]

Melt Pool Discontinuity

Another common source of defects is the lack of continuity in the melt pool. This occurs when the used energy density is not high enough or the hatching distance is too large. This causes less or no overlap of the melting pool between hatch lines. In these situations there is a change in wetting and thermal conduction of the melt pool. If the molten material fails to wet the previous layer and/or hatch line, it is thus insulated by surrounding powder and slower cooling enables surface tension effects to give rise to voids and pores. A typical discontinuity between melt pools is shown in fig. 2.7.

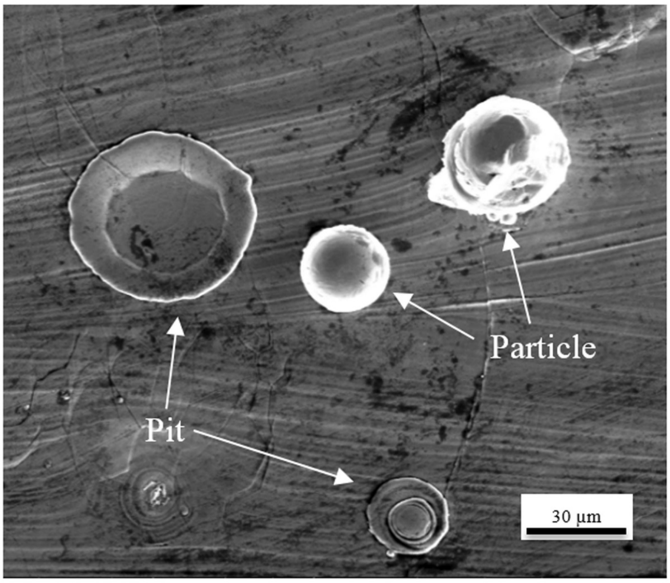

Figure 2.6: Defects caused by mass transfer showing both the welded particles and the pits where removed particles were. [18]

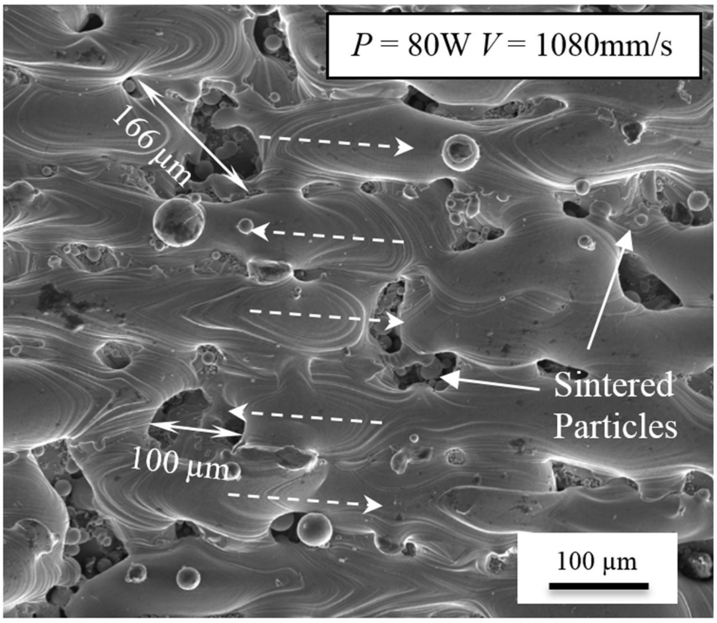

Figure 2.7: Melt pool discontinuity in a Ti-6Al-4V sample. [18]

2.2 Titanium and its Alloys in L-PBF

In past years, Titanium based-materials have found their way into multiple industries as a crucial building material due to their wide variety of advantages among which are: low density, superior corrosion and erosion resistance and high temperature capability (300-600 °C). However these also have some drawbacks the most significant being its cost.

2.2.1 Microstructure

At room temperature, pure Titanium, takes a modified hexagonal close compacted structure (HCP) (α) but at a temperature of 883 °C it undergoes a transformation to a body centred cubic phase (BCC) (β) which then remains stable up to the melting point of 1678 °C.

They can be classified based on their microstructure by the following categories: α, near-α, α+β, near-β, metastable β and stable β. α and near-α alloys mainly have α structure but may possess different microstructural grain morphologies ranging from acicular to equiaxed and are preferred for higher temperature applications. β titanium alloys contain a balance of β stabilisers to α stabilisers which is sufficient to ensure that a fully β phase microstructure can be retained on fast cooling (slow cooling, in furnace, causes β-phase decomposition). In this condition, the metastable β alloys are generally thermodynamically unstable. As a result, the metastable β titanium alloys generally have higher strength, higher toughness and improved formability at room temperature as compared to the α and α + β titanium alloys. The metastable β alloys are heat treatable to very high strength usually by solution treatment plus quenching followed by ageing. The highest strength among titanium alloys can be reached with such heat treatment combined with cold deformation. [19]

Equiaxed α grains are usually developed by annealing cold-worked alloys above the recrystallization temperature. As the cooling rate increases, the lamellar α becomes finer. Generally, two types of α – primary α and secondary α or transformed β – are present. The primary α is present during prior hot working, remnants of which persist through heat treatment. The secondary α is produced by transformation from β. This may occur upon cooling from above the β-transus or high within the α + β phase field, or by aging of the β. The α in these areas has different appearances and may be acicular or lamellar, platelike, serrated, or Widmanstätten.

Acicular or lamellar α is the most common transformation product formed from β during cooling. It is a result of nucleation and growth on crystallographic planes of the prior β matrix. Precipitation normally occurs on multiple variants or orientations of this family of habit planes. A packet or cluster of acicular α grains aligned in the same orientation is referred to as a ”colony.” When correlating this type of microstructure with properties such as fatigue or fracture toughness, colony size is often regarded as an important microstructural feature. The multiple orientations of α have a basketweave appearance characteristic of a Widmanstätten structure. Lamellar α forming from small β grains may have a singular orientation.

Unless heat treatments are performed in an inert atmosphere, oxygen and nitrogen will be absorbed at the surface, stabilize the α, and form a hard, brittle layer referred to as an "α case". This case is normally removed by chemical milling or machining. A part should not be put into service unless this α case has been removed.

Martensite is a nonequilibrium supersaturated α-type structure produced by diffusionless transformation of the β. There are two types of martensite: α', which has a hexagonal crystal structure, and α", which has an orthorhombic crystal structure. Martensite can be produced in titanium alloys by quenching or by applying external stress. α' can only be formed by quenching. Aging of the martensite results in its decomposition to α + β.

In α + β and β alloys, some equilibrium β is present at room temperature. A nonequilibrium, or metastable, β phase can be produced in α + β alloys that contain enough β-stabilizing elements to retain the β phase at room temperature on rapid cooling from high in the α + β phase field. The composition of the alloy must be such that the temperature for the start of martensite formation is depressed to below room temperature. One hundred percent β can be retained by air cooling β alloys. The decomposition of this retained β (or martensite, if it forms) is the basis for heat treating titanium alloys to higher strengths. [20]

A summary of the relation between the mechanical properties and the part's microstructure can be found in table 2.1.

2.2.2 The Ti-6Al-4V Alloy

Ti-6Al-4V is an α+β type Titanium alloy [20] and is presently the most widely used high-strength titanium alloy, covering over 60% of Titanium alloys produced in the USA and the EU [21]. It finds a large application in the aerospace industry and in medicine, for medical prostheses. It is also used in the automotive, marine and chemical industries. Its chemical composition can be found in figure 2.8. Its two other main elements are Aluminum and Vanadium. The Aluminum acts as an α-phase stabilizer and strengthener, i.e., it increases the temperature at which the α phase is stable and reduces alloy density. On the flip side, Vanadium is a β stabilizer which means that it increases the stability of the β phase at lower temperatures and facilitates hot working. [20, 21]

When produced using L-PBF methods, Ti-6Al-4V parts predominantly show α' martensite microstructure [22–24] due to the rapid heating and cooling cycles (10^3 - 10^8 K/s [17]) that result from the several passages of the laser on the melt pool and on subsequent layers. [25] This is in line with the CCT diagram for Ti-6Al-4V. This can be seen in figure 2.12. Elongated prior-β grains can also be seen in the side view of the figure. They grew epitaxially and span over multiple layers. This is because the dissipation of heat occurs by conduction through the substrate in the first layer. [26] The width of these grains matches the hatch distance used in the process. It has also been found that the local heat conduction (which is affected by the scan strategy) affects the orientation of the martensite structure.

Feature	Enhances	Degrades
Equiaxed α	Strength, ductility, fatigue initiation resistance, LCF resistance	Fracture toughness, fatigue crack growth resistance, notched fatigue resistance
Elongated α	Fracture toughness, fatigue crack growth resistance, notched fatigue resistance	Ductility, fatigue initiation resistance, LCF resistance
Widmanstätten α/α-plates	Fracture toughness, fatigue crack growth resistance, notched fatigue resistance, creep	Ductility, fatigue initiation resistance, LCF resistance, strength
Colony α	Fracture toughness, fatigue crack growth resistance, notched fatigue resistance	Strength, ductility, fatigue initiation resistance, LCF resistance
Grain boundary α	Fracture toughness, fatigue crack growth resistance, notched fatigue resistance	Ductility, fatigue initiation resistance, LCF resistance
Elongated grain shape	Fracture properties, fatigue crack growth resistance, notched fatigue resistance	Fatigue initiation resistance
Coarse prior β grains	Fracture toughness, creep	Strength, ductility, fatigue initiation resistance, LCF resistance

LCF - Low Cycle Fatigue

Table 2.1: Selected microstructural features and effect on properties of titanium alloys. [27]

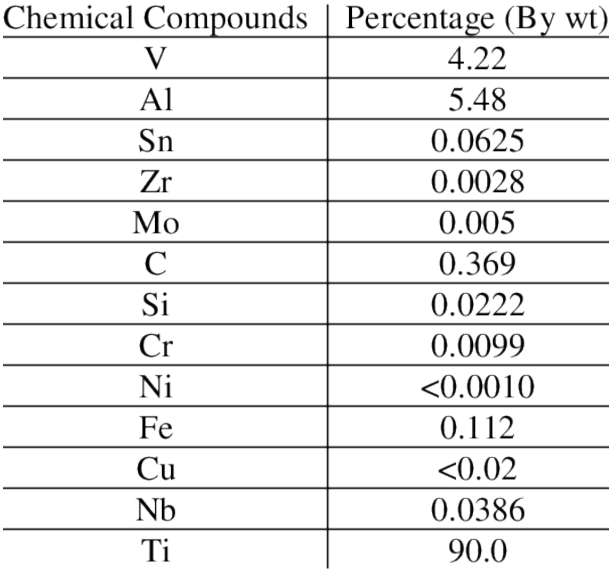

Chemical Compounds	Percentage (By wt)
V	4.22
Al	5.48
Sn	0.0625
Zr	0.0028
Mo	0.005
C	0.369
Si	0.0222
Cr	0.0099
Ni	<0.0010
Fe	0.112
Cu	<0.02
Nb	0.0386
Ti	90.0

Figure 2.8: Chemical composition of Ti-6Al-4V. [28]

It's important to note that while most L-PBF produced Ti-6Al-4V parts do exhibit α' martensitic microstructure, not all do. Pre-heating the powder bed and increasing the layer thickness produces a different microstructure, as shown in figure 2.10. [17]

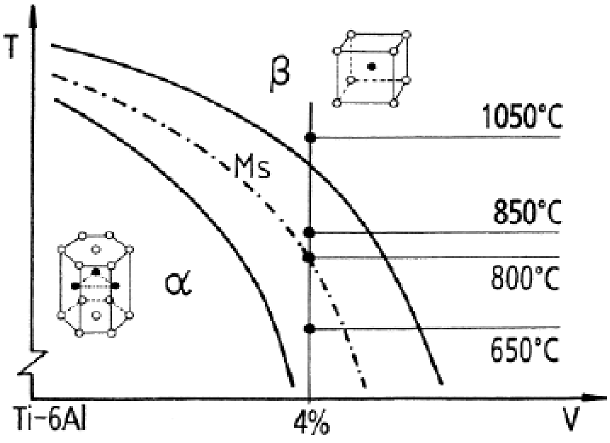
T
β
1050°C
Ms
850°C
800°C
α
650°C
Ti-6Al
4%
V

Figure 2.9: Phase diagram of Ti-6Al-4V. [29]

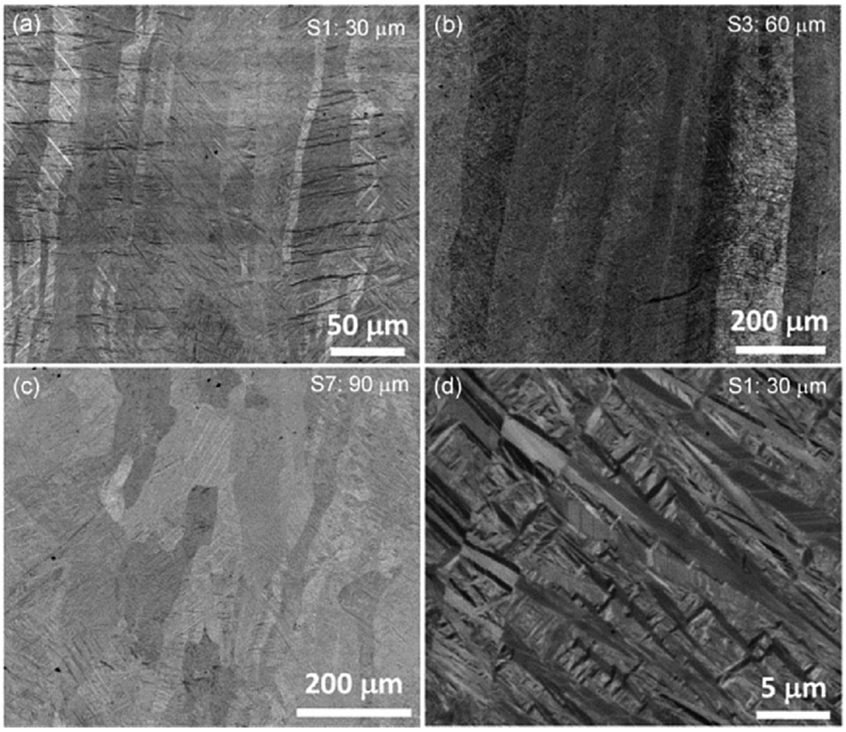
(a)
S1: 30 μm
50 μm
(b)
S3: 60 μm
200 μm
(c)
S7: 90 μm
200 μm
(d)
S1: 30 μm
5 μm

Figure 2.10: L-PBF produced Ti-6Al-4V a) Columnar prior-β grains filled α' martensite with 30 μm layer thickness b) ultrafine lamellar $\alpha + \beta$ structure with 60 μm layer thickness c) acicular α' with minor $\alpha + \beta$ lamellae using a layer thickness of 90 μm, d) detail of a). [21]

Heat Treatment

As referred in the previous section, as-produced Ti-6Al-4V parts produced in L-PBF will usually have a fully acicular α' martensitic microstructure, with no presence of β phase. From here, these parts can be left as they are or heat treated which would consist of one or more cycles of heating and/or cooling.

Various types of heat treatment exist. When heating with a regular airtight furnace, the different types of heat treatment can be classified according to their purpose (which can consist of changing the microstructure of the piece or to mitigate any defects it may have) and the temperature [21]:

- **Aging** - A change in properties that occurs at ambient or moderately elevated temperatures after hot working, heat treating, or cold working. The change in properties is often due to a phase change (precipitation), but does not alter chemical composition. This can occur naturally throughout the years or can be forced by subjecting the part to high temperatures.
- **Annealing** - A generic term denoting a treatment – heating to and holding at a suitable temperature followed by cooling at a suitable rate – used primarily to soften metallic materials, but also to produce desired changes simultaneously in other properties or in microstructure.
- **Solutioning** - It can be described as the heating of an alloy to a suitable temperature, holding it at that temperature long enough to cause one or more constituents to enter into a solid solution and then cooling it rapidly enough to hold these constituents in solution. It increases the strength of the parts by producing precipitates of the alloying material within the metal structure. [20]

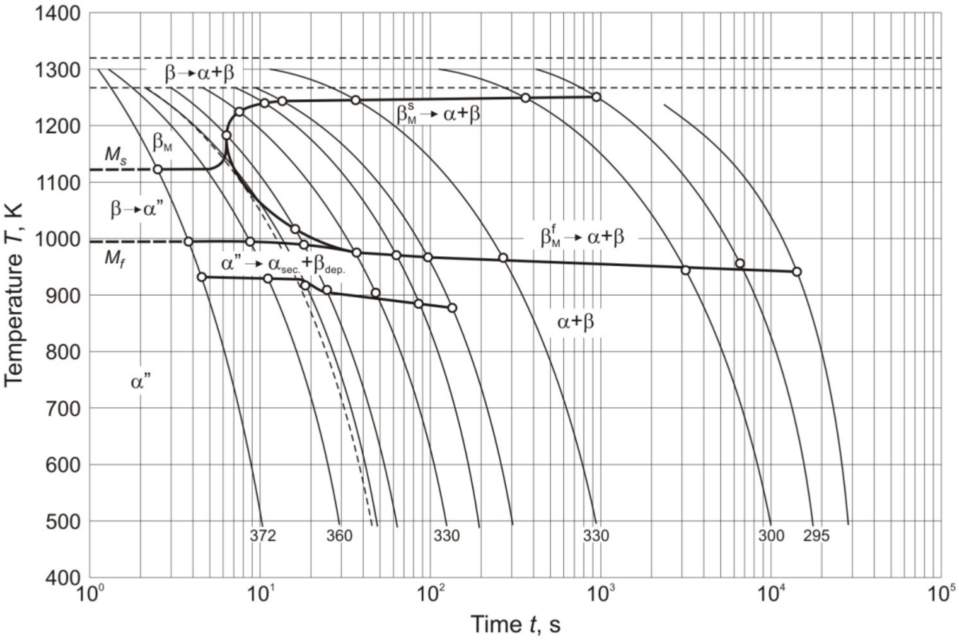

Figure 2.11: CCT diagram of Ti-6Al-4V. [21]

For Ti-6Al-4V parts, heating can be done in the 400 °C-1200 °C temperature range and with a residence time that can go from as little as 20 minutes to as long as 20 hours and sometimes more. As for the cooling, there are 3 main methods: water quenching where the piece is dipped in water (fastest method), air cooling where the piece is cooled either in still air or with the aid of some device that ensures air flow and furnace cooling where the piece is left inside a furnace and is allowed to cool at a set rate.

The temperatures at which the parts can be treated can be divided into two main intervals: below the β-transus, sub-transus, and above the β-transus, super-transus. For most cases and depending on the small variations of the alloy's composition, the β-transus is usually located at around 1000 °C. The final properties of the part are dependant on the balance of α and β grains and their geometry. Since the initial structure is usually comprised of the aforementioned α' grains, it makes sense to first evaluate how these behave when submitted to heat treatment. When heated, the α plates become coarser and reduce in terms of fraction. This means that the percentage of β grains increases as the temperature approaches the β-transus at which point there are no more α plates. Beyond the β-transus, the microstructure takes the form of equiaxed β grains and completely clears the L-PBF footprint. When a super-transus heated part is water quenched the same α' martensitic microstructure is created again but it is now thicker due to the slower cooling rate when compared to the one verified during L-PBF production. It is also worth noting that it also erases the columnar structure whereas sub-transus treatments keep it. [26]

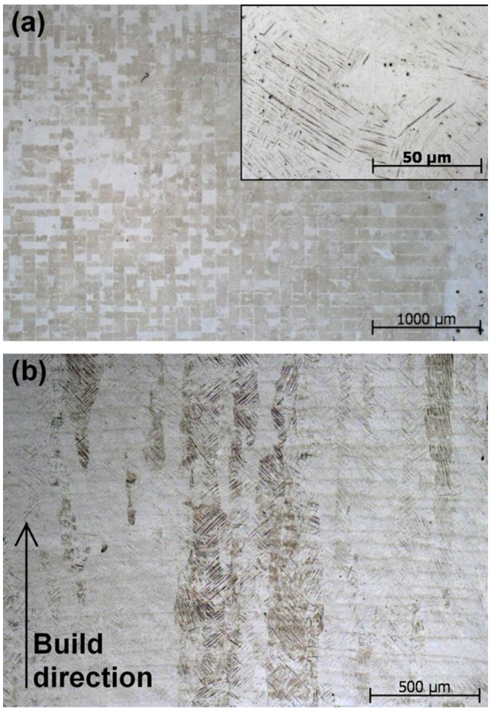

Figure 2.12: Top (a) and side (b) view of untreated Ti-6Al-4V produced by L-PBF. The chessboard pattern is due to the scan pattern used to produce this part. Columnar prior-β grains can also be seen in the side view. [30]

In general, its been noted that the material reacts differently to different factors depending on whether its starting temperature is above the β-transus or not. Below it, the main factor that affects the microstructure is the sitting temperature. As mentioned before, treatments done at higher temperatures lead to a small percentage of α grains. This can be seen in figure 2.13. Above the β-transus, the residence time and the heating/cooling rates are the main affecting parameters. The longer the residence time is and the slower the heating/cooling rates are the larger the grains will be. This is because the slower changes in temperature allow the grains more time to grow. The heating/cooling rate can also affect the morphology, but to a lesser extent. High cooling rates such as those obtained through water quenching (410 °C/s) would lead to an α' martensitic structure similar to the one obtained from as-built parts. Lower cooling rates produce lamellar α + β from the equiaxed β grains. It is also worth noting that the maximum size of an α colony is limited by the size of the β grain in which it originates. [30]

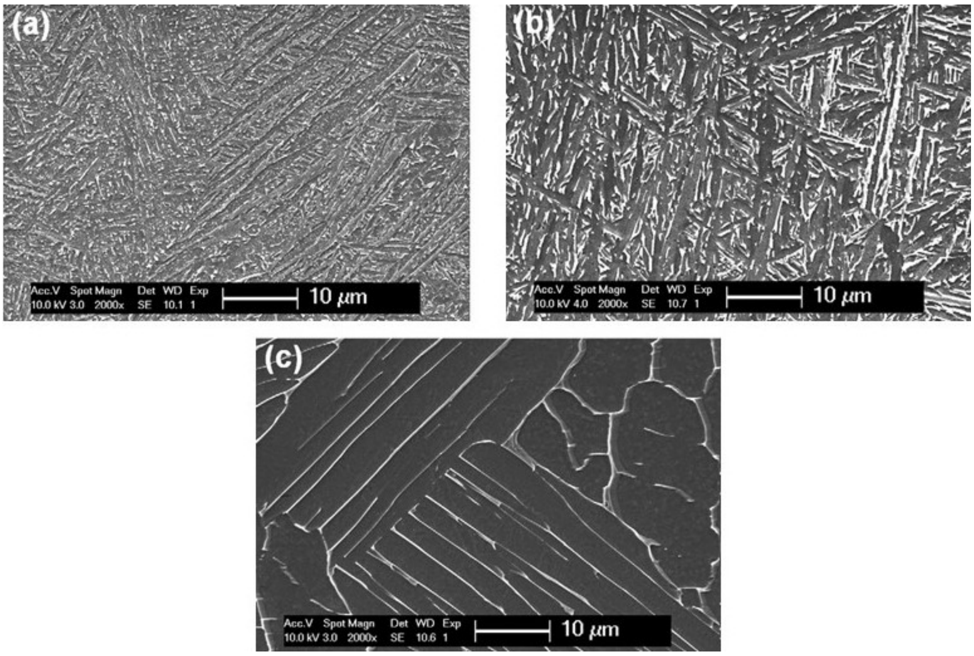
(a)
Acc.V Spot Magn Det WD Exp
10.0 kV 3.0 2000x SE 10.1 1
10 μm
(b)
Acc.V Spot Magn Det WD Exp
10.0 kV 4.0 2000x SE 10.7 1
10 μm
(c)
Acc.V Spot Magn Det WD Exp
10.0 kV 3.0 2000x SE 10.6 1
10 μm

Figure 2.13: Microstructure of Ti-6Al-4V produced by PBF after heat treating at different temperatures for 2 h, followed by furnace cooling. (a) 780 °C (b) 843 °C (c) 1015 °C. Lighter zones are β phase, the dark phase is the α phase. [30]

Hot Isostatic Pressing While hot isostatic pressing, otherwise known as HIP or hipping, is not going to be used as a heat treating process for this thesis, it is important to keep in mind as an alternative to conventional heat treating processes as it yields different results.

Hot isostatic pressing, as the name denotes, consists of heating a part or a material at a certain temperature and at a certain constant pressure. The pressure within the chamber is obtained through a combination of a mechanical compressor and the heating of a gas within a closed space. Under certain conditions, this causes the gas atoms or molecules to bounce off of the surface of the part at speeds of 900 m/s and about 10^{30} collisions to occur with the part per square meter, per second. These collisions act as atomic hot forges that affect every single surface of the component at a normal direction. [31]

HIP has a wide variety of uses that go from producing dense components from powdered metals and ceramics to bonding materials that would otherwise be impossible to bond without the multiplier effect from the isostatic pressure and high temperature. [32] However, in this situation, hipping is used due to its ability to compact the pores generated during the SLM process and altering the microstructure. [33] When applied to SLM, the hipping parameters are usually as follows: pressures ranging from 100 MPa to 130 MPa, temperatures ranging from 920 °C to 930 °C, sitting times ranging from 2 to 4 hours and are cooled within the furnace at a slow rate. [33–36]

From a general perspective, hipping with these parameters yields similar or slightly lower results for UTS and yield strength to those of heat treated parts but with slightly better elongation values and considerable improvements in fatigue applications. The microstructure usually consists of lamellar and polygonal α grains and intergranular β phase. [35]

Mechanical Properties

The general consensus among the literature is that in two phase titanium alloys with lamellar microstructure, the thickness of α lamellae and diameter of their colonies as well as the maximum heat treatment temperature are the most important parameters relating to mechanical properties. [21, 30] A closer look at the lamellar microstructure can be found in figure 2.14. There's a tendency for yield strength and UTS to decrease with the increase of thickness and colony size of parallel α phase lamellae. Finer microstructures also result in harder parts. [26]

When heat treated at around 500 °C, also known as age hardening, the mechanical properties of Ti-6Al-4V parts are improved due to fine precipitation of Ti_3Al, at the cost of lower fracture strain and lower ductility. [37] In as-built parts, usually, the columnar grains will be favored for creep tests, whereas equiaxial grains will be preferred for fatigue tests. [38]

Parts produced through L-PBF are usually very anisotropic regardless of their microstructure or the heat treatment they've been submitted to [13]. This is due to the manufacturing defects and their orientation. Reduction of layer thickness and scanning speed along with increased laser power help to mitigate their effects. [26]

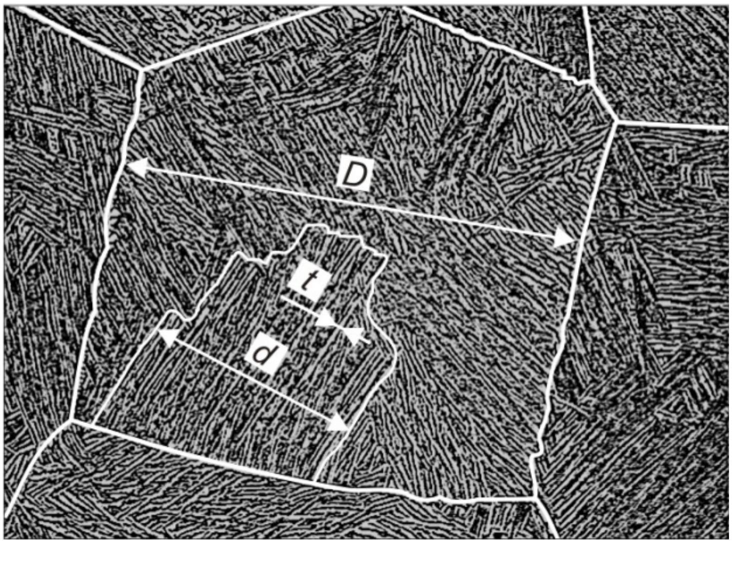

Figure 2.14: Stereological parameters of lamellar microstructure: D – primary β-phase grain size, d – size of the colony of parallel α-lamellae, t – thickness of α-lamellae. [21]

Tensile Properties B. Vrancken et al. conducted a series of tests [30] where they tried different heat treatments on T-6Al-4V parts produced in L-PBF with varying temperatures (540 °C to 1020 °C), residence times (0.5 h to 5 h) and cooling rates (WQ, AC and FC). They also measured some of the samples' mechanical properties allowing us to draw conclusions from these results. A direct correlation was noted between the maximum temperature used in the heat treatments and the fracture strain/yield strength. The higher the used temperature was, the higher the fracture strain and the lower the yield stress were. This means that higher temperatures produce more ductile parts. These results confirm the literature. Higher temperatures closer and above the β-transus reduce the percentage of α grains in the part. The lower amounts of α and the high temperature mean they are coarser resulting in a more ductile part. [30] This was verified also because the cooling method allowed it to. A very high cooling rate, i.e water quenching, would've resulted in a finer microstructure almost regardless of the temperature used in the heating process. Since furnace cooling and air cooling were used for most tests, this was not the case. The only test where water quenching was used resulted in the most brittle sample.

This test also stresses the importance of knowing the original microstructure of the part and what the objectives of heat treating are because the results can vary greatly. This is because they performed the same tests on wrought Ti-6Al-4V parts which resulted in completely different results from the parts produced with L-PBF. While the yield remained practically unaffected by the heat treatments, the fracture strains seemed to be inversely affected. Lower temperatures yielded more ductile parts.

The conclusion reached was that for L-PBF produced Ti-6Al-4V parts, heat treating at intermediate to high temperatures below the β-transus, followed by furnace cooling proved to be optimal for an overall optimization of tensile properties.

In general, HIPed parts exhibit tensile properties akin to those that have been treated in a traditional oven except for elongation. HIPed parts end up with a noticeably larger value for elongation. This is not only due to the formation of larger α grains but also because the process removes and reduces the sizes of pores in the part and thus removing possible failure mechanisms. [39]

Hardness Vilaro et al. ran tests [26] on parts that had been treated at a supertransus temperature and water quenched (1050 °C/1h WQ). This ensured that the parts had a similar α' martensitic structure with no sign of being produced through L-PBF. Then, they were treated at different temperatures in the 700 °C to 950 °C range for 2 hours and then air/furnace cooled. The results can be seen in figure 2.15.

The sudden dip in hardness in the air cooled samples from 800 °C to 850 °C is due to the formation of the soft orthorhombic martensite α". From figure 2.15 it is easy to see that the treatment that yielded the hardest sample was 1050 °C/1h WQ + 800 °C/2h FC.

As there aren't many (if any other) articles studying the effect of heat treatments on the hardness of L-PBF printed Ti-6Al-4V, any other predictions regarding these results will have to be derived from the effects on other values that have been observed to be correlated, like UTS.

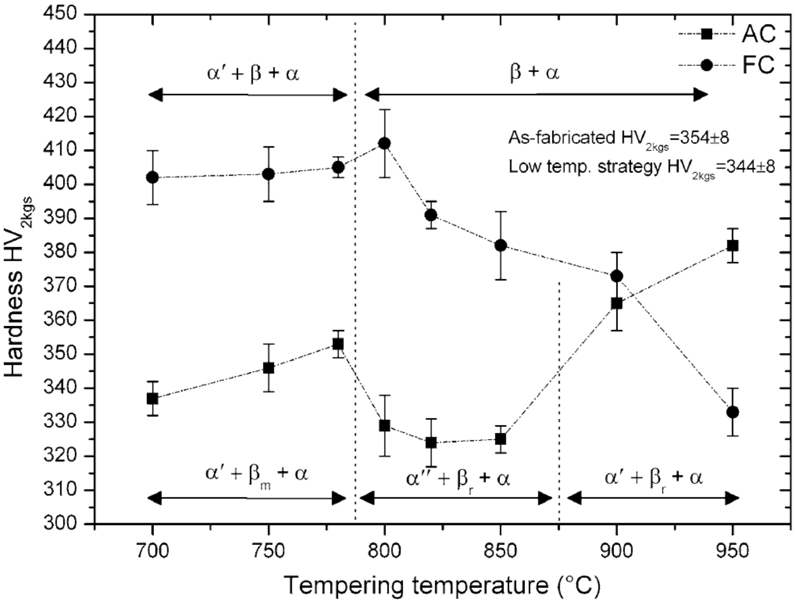

Figure 2.15: Hardness evolution of the Ti-6Al-4V microstructure as a function of the tempering temperature after a solution treatment at 1050 °C during 1 h WQ, for both air and furnace cooling. [26]

Fatigue Behaviour The main factor that affects the fatigue behavior of an L-PBF produced part is its surface roughness which is mostly affected by the part geometry and L-PBF build parameters. Other factors include microstructure, defects and build orientation. [40, 41] Heat treating the part can affect all factors except for the build orientation.

The fatigue life of a metallic material consists of two main parts: the crack initiation and the crack propagation. Firstly, the crack initiation starts from pores produced by the L-PBF process. The crack will normally initiate from pores on the surface or from inner pores if the surface is polished. While the HIP process can help to correct these problems, traditional heating does not have a great effect so the crack initiation mechanisms will not vary greatly. However, the crack propagation does significantly slow down for heat treated parts. This is, once again, due to the coarser α laths which result in larger effective slip lengths and an increase in the ductility of the material. These results were confirmed in a test done by Yu et al. [39] where they compare results obtained from an as-built part, a HIPed part and two heat treated parts (figure 2.16).

For high stress amplitudes, all parts maintain relatively similar behaviors. But as we approach the fatigue limit, an improvement of about 50 to 100 MPa can be observed and that the parts can withstand a greater amount of cycles until failure. However, these fatigue properties are still below those found in its wrought variant.

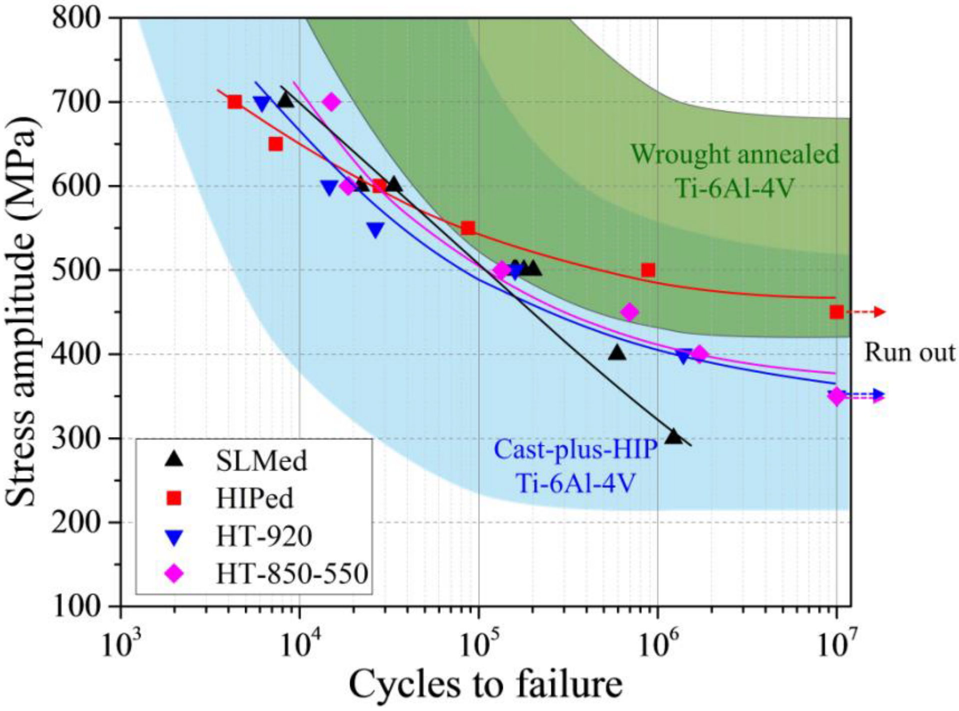

Figure 2.16: Fatigue performances of SLMed, HIPed, HT-920 and HT-850-550 Ti-6Al-4V specimens. [39]

2.2.3 Typical Defects

As mentioned in section 2.1.4, there are a number of defect creation mechanisms that occur during the printing process resulting in many defects that affect the mechanical properties of the final components. This section aims to give a general overview of what types of defects exist and how to mitigate or correct them.

Lack of Fusion

Lack of fusion is described as being the improper melting of a new layer over the previous one, usually due to poorly optimized printing parameters. This results in discontinuous sections with irregular shapes where there may exist unmelted powder particles and can reach sizes up to 500 μm [42]. This negatively affects the component's mechanical properties, especially the fatigue life and can cause delamination of layers, which makes sense given that these defects occur between layers.

The way of mitigating these kinds of defects is to ensure better binding between layers. This can be achieved by decreasing the layer thickness or increasing energy density. Heat treating at temperatures above 700 °C [43] could cause the unmelted particles to sinter, partially filling in some gaps and improving continuity, but never completely solving the problem.

Gas Pores

Gas pores are generated due to gas entrapment during the printing process. This happens within the melt pool and stays within it due to the high cooling rates. The entrapped gas comes from the atmosphere and from the vaporised constituents of the material with the lowest melting points. Similarly to defects caused by lack of fusion, these present as porosity in the material. However, this results in spherical pores with sizes ranging from 5 to 80 μm and are considerably more common [42]. These lower the part's density and worsen its tensile and fatigue properties. With gas pore densities up to 1 % the mechanical properties aren't significantly affected, however, they considerably worsen once it reaches values above 5%. [18]

These defects can be reduced through reducing the volume of liquid metal, reducing the layer thickness, decreasing gas pressure or increasing the powder bed density. At a surface level, shot peening and hipping can also be used. Although performing L-PBF in a vacuum is not a necessity, doing so has shown to reduce porosity in as-built parts. [44]

Anisotropy

The anisotropy characteristic to components produced through L-PBF stems from the way they are oriented during the printing process. For instance, if regular bone-shaped tensile testing coupons were to be printed flat, on the edge or vertically in the same print and with the same parameters, they would present different tensile properties. The flat printed would warp due to strong heat variations and the vertically printed samples would present the weakest properties due to the orientation of the microstructure in relation to the applied load. In this last case, fractures would occur intergranularly along the boundaries of the prior-β grains, which grow in the build direction, due to the crack paths and rougher fracture surface profiles generated there. [13]. As referred in section 2.1.3, there can be reductions of about 10 to 13% in UTS and YS values. The only way of solving this issue is by printing the part oriented in the way that best counters its real world loading situations.

Residual Stresses

Residual stresses are caused by high thermal gradients, which are inevitable in SLM. These can form stress concentration pockets which can lead to premature brittle failure. [45] This type of defect can be corrected by subjecting the components to heat treatments which can completely remove any evidence of the residual stresses. [46]

Poor Microstructure

The microstructure is one of the most important aspects of L-PBF printed parts and has already been extensively developed upon in section 2.2.1. In summary, the α' martensitic microstructure that the as-built parts present is usually undesirable due to its fragile nature and heat treatments are done to modify its microstructure and, therefore, mechanical properties. Usually, the maximum elongation is greatly increased while the UTS and YS are slightly decreased after heat treatment.

Balling

The balling phenomenon takes place when the total melt-pool surface becomes larger than that of a sphere containing equivalent volume and is enhanced if the melt-pool's viscosity is too low or there's excessive molten material aggregation. [47, 48] The only way of reducing these defects is by optimizing printing parameters, namely the energy density. This type of defect mainly affects the fatigue properties. [49]

Surface Roughness

As-built parts are always produced with high surface roughness due to the nature of their building process and the fact that they are produced from powder. The main printing parameter associated with surface quality is the melt pool overlap as the higher it is, the smoother the surface. [18] Using an ELI powder can also improve surface roughness. However, the best way of solving this defect is through post-processing, like polishing. The rough surface can act as crack initiation points and stress concentration areas, causing a deterioration in mechanical properties in general. The surface roughness has been reported to reach values up to $R_a = 17.9\mu m$ on slanted surfaces. [50]

Hot Tears

The existence of hot tears in the L-PBF products is a consequence of the existence of the stresses and high temperature. Hot tears can exist in variety of materials produced with L-PBF. The tears are more critical at elevated temperatures and found to menace during commercial use. Since these occur at high temperatures, the best solution for avoiding them is by avoiding such temperatures. [51]

Fish Scales

Fish scales are a type of microstructural discontinuity. These are formed through solute concentrations during layer by layer solidification of the powders in the L-PBF process. Variations in precipitate formation and morphology are also the major reasons behind their existence. Fish scales are always perpendicular to the heat flow direction via conduction. These may result in delamination and the only way of avoiding them is through proper printing parameter selection. [52]

Chapter 3

Experimental Approach

3.1 Overview of the Experimental Approach

The experimental approach consists of producing Ti-6Al-4V testing coupons through Laser - Powder Bed Fusion, heat treating them at different parameters and then testing them and analyzing the results.

According to the DOE, groups of 3 testing coupons were subjected to heat treatments with different combinations of parameters. These heat treatments vary according to the sitting temperature, the sitting time and the cooling rate and will all occur in an inert atmosphere. Each of these parameters have 3 different values each, and would result in a total of 27 different sets of values.

However, after a misunderstanding by the company performing the heat treatments, it was revealed that one of the cooling methods was wrongfully used. One third of the coupons were oil quenched as opposed to air cooled. As this was thought to not yield the desired results for the subsequent analysis, it was agreed that two thirds of the affected coupons (18 out of the 27) would be reheated with the same established parameters and cooled with the originally planned method, air cooling. This resulted in 36 different sets of parameters.

Following the treatments, they were subjected to mechanical testing, namely hardness tests and tensile testing. Aside from these heat treated coupons, 5 more as-built coupons were subjected to the same mechanical tests for comparison. This brought the total testing coupons to 86.

In figure 3.1, a flowchart representing the main steps in the experimental approach are schematized.

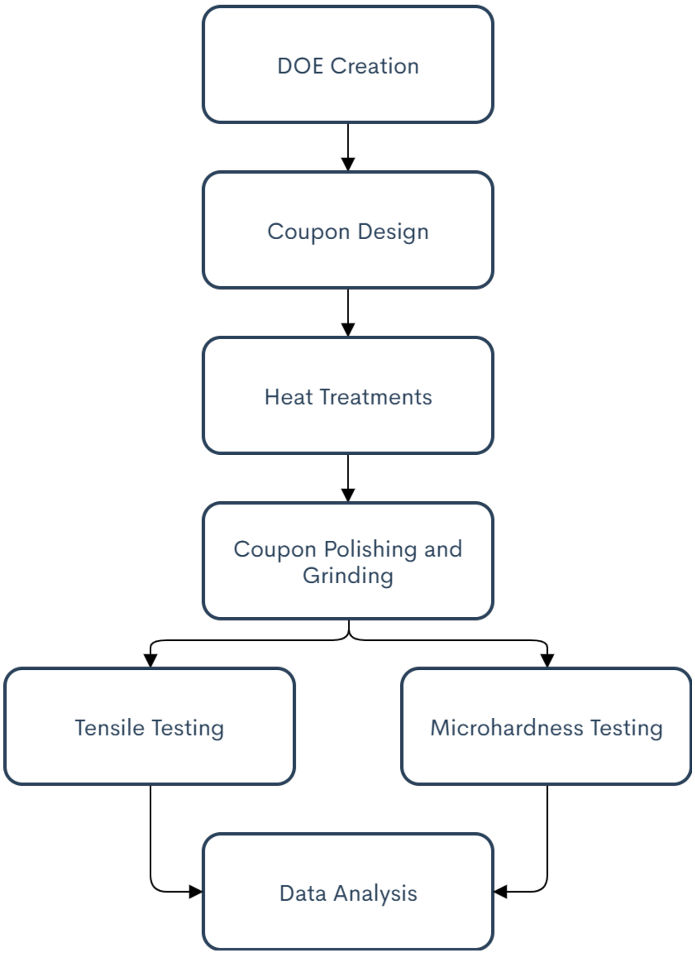
DOE Creation
Coupon Design
Heat Treatments
Coupon Polishing and Grinding
Tensile Testing
Microhardness Testing
Data Analysis

Figure 3.1: Flowchart of the experimental approach.

3.2 Material

The material used was Ti-6Al-4V Grade 23 Powder from AP&C produced by plasma atomization, with a density of 2.52 g/cm^3 and a particle size ranging from 10 to 45 μm. The material composition and the size distribution of the powder can be found in tables 3.1 and 3.2.

It's relevant to point out that the normal density value for this material is of about 4.41 g/cm^3 [53]; there is a very large gap in the density value of the powder provided and the theoretical one.

3.3 Printing the Coupons

The machine and computer program used to print the parts were the RenAM 500PM and QuantAM from Renishaw at IMR. The coupons were laid out vertically in a grid of 8 rows and 11 columns adding to a total of 88 as shown in figure 3.2, 86 of which were used for this thesis. These were all printed at once in order to save time and resources.

Material	Amount [Wt. %]
Aluminum, Al	6.44
Vanadium, V	3.91
Iron, Fe	0.20
Oxygen, O	0.13
Carbon, C	0.01
Nitrogen, N	0.01
Hydrogen, H	0.002
Yttrium, Y	$<$0.001
Other Each	$<$0.08
Other Total	$<$0.20
Ti	Balance

Table 3.1: Composition of the powder used to produce the testing coupons according to the manufacturer.

Dimension [μm]	Composition [%]
$>$ 63	0.0
$>$ 45	2.6
$<$ 45	97.3

Table 3.2: Size distribution of the powder according to the manufacturer.

The coupons to be printed are the subsize specimens according to standard ASTM E8 with a thickness of 4 mm, a width of 6 mm and a length of reduced section of 32 mm. An example of one, still shown in the print bed, can be seen in fig 3.3.

As for the printing parameters, which are shown in table 3.3, these were chosen based on a previous master's dissertation [54] performed to optimize the printing of parts made from the same material in the same printing machine.

Parameter	Value
Laser Diameter [μm]	75
Laser Frequency [kHz]	100
Power [W]	200
Layer Thickness [μm]	60
Total Layers	1666
Scanning Strategy	Stripe
Point Distance [μm]	60
Exposure Time [μs]	70
Angle Between Layers [º]	67
Hatch Spacing [μm]	95
Volumetric Energy Density [J/mm^3]	40.935

Table 3.3: List of the main printing parameters.

3.4 Design of Experiments

In table 3.4, the DOE for the production of the aforementioned testing coupons is shown presenting the specific values for the parameters of the heat treatments. Evaluating the behaviour of the Ti-6Al-4V near the β-transus (1000 °C) was a priority, so temperatures immediately above and below it were chosen

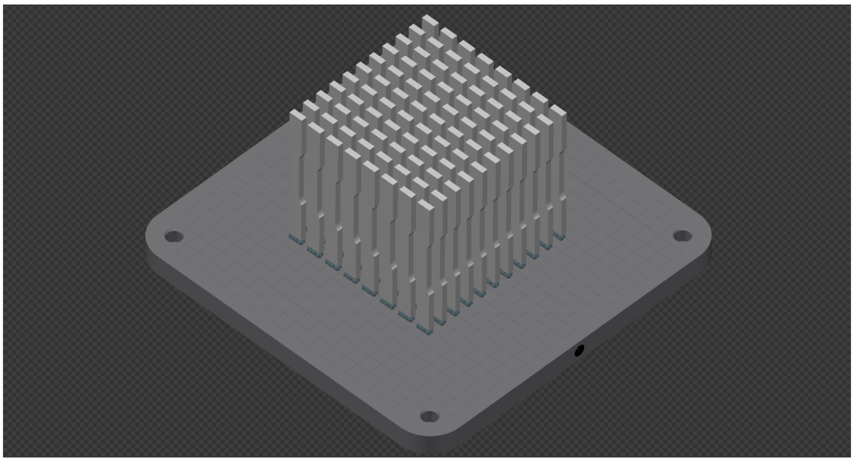

Figure 3.2: The print layout of the testing coupons viewed in the software.

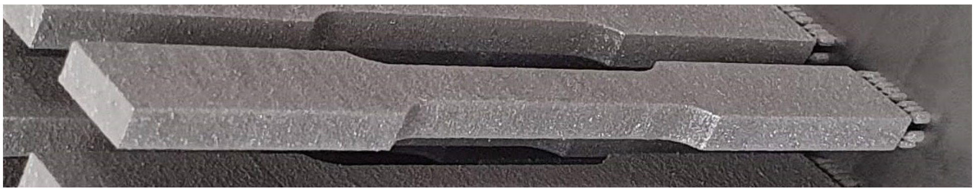

Figure 3.3: As-built coupon still attached to the print bed with supports visible.

(950 °C and 1100 °C). The remaining values were chosen as they seemed to be within the range of most commonly used parameters in the literature and the most relevant to develop on [26, 30, 35].

Factor	**Name**	**Units**	**Low Level**	**Middle Level**	**High Level**
A	Resting Temperature	°C	800	950	1100
B	Resting Time	hours	0.5	3	5
C	Cooling Rate	-	Furnace Cooling	Air Cooling (after oil quenched)	Water/Oil Quenching

Table 3.4: Design of Experiments.

As previously explained, the original DOE consisted solely of 3 different levels for each parameter leading to 27 different combinations evenly spread through 81 coupons. However, after mistakenly oil quenching the coupons that were supposed to be air cooled (27 coupons), it was decided to keep one third of them as they were (9) and to repeat the originally planned heat treatment for the rest (18). This means that, in the end, there are 36 different parameter combinations: 18 of those represented in 3 coupons (the water quenched and furnace cooled), 9 in 2 coupons (oil quenched then air cooled) and 9 in 1 coupon (oil quenched). A full list of the different combinations of parameters can be found in appendix A.1.

3.5 Equipment

3.5.1 Coupon Design

The testing coupons were designed according to the ASTM E8 standard using the software Magics at IMR. This software was used for its features, among which are the ability to prepare the .STL files for use in AM by accounting for support structures.

3.5.2 L-PBF Printing System

The 3D printer used for this thesis was the RenAM 500M (figure 3.4) developed by Renishaw. It has a 500 W ytterbium fiber laser and a 250 mm x 250 mm x 350 mm build volume. It also contains features such as on board sieving and powder recirculation as well as a dual SafeChange filter that automatically senses and redirects recirculation gas to maintain optimal performance and chamber cleanliness.

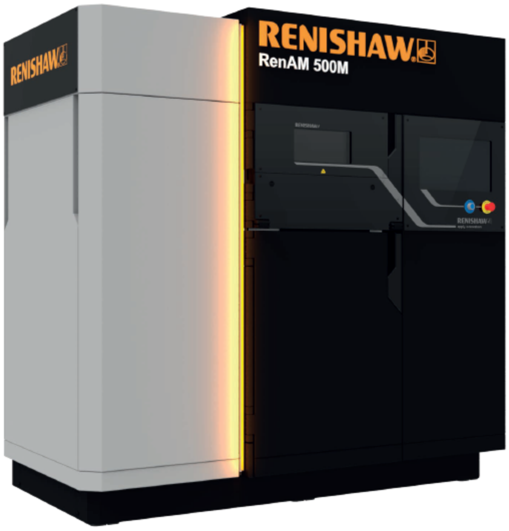

Figure 3.4: The Renishaw RenAM 500M.

This 3D printer works in tandem with the QuantAM software provided by the same company which allows for the preparation of parts for 3D printing.

3.5.3 Heat Treatments

The heat treatments for this thesis were done in collaboration with the Material Services branch of the company Thyssenkrupp in Marinha Grande, Portugal. The heat treatments were done in ovens with no atmosphere, i.e., in a vacuum.

3.5.4 Polishing and Grinding

The polishing and grinding of the testing coupons were done using a Struers LaboPol-30 (fig. 3.5) for wider sides and a Multi 395 Dremel with a grinding tip for the narrow sides.

While polishing, the discs were rotating at 500 rpm and the coupons were actively cooled through a stream of water.

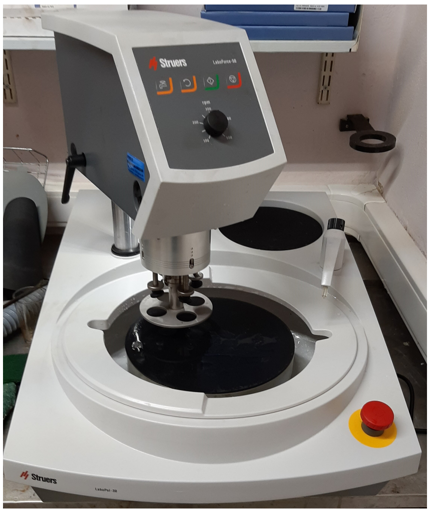

Figure 3.5: The Struers LaboPol-30 used to polish the samples.

3.5.5 Tensile Testing

The tensile testing was performed using an Instron 4507 (fig. 3.7) with a 200 kN load cell and a Static Axial Clip-On Instron Extensometer. A custom part was designed and 3D-printed to be used with the extensometer because the base model was too large to be used with the coupons. The extensometer can be seen with the new part in figure 3.6.

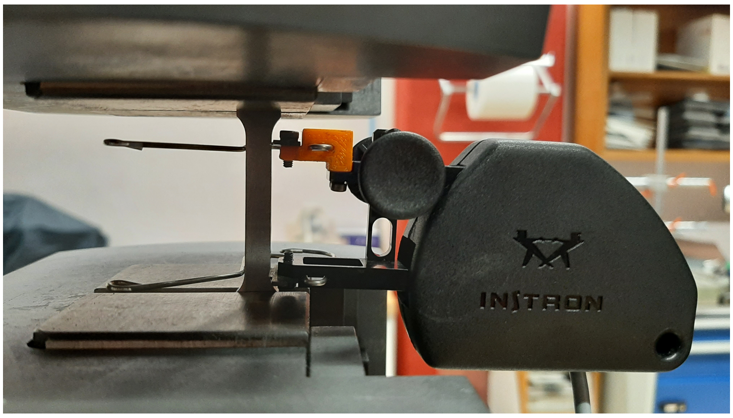

Figure 3.6: The Static Axial Clip-On Instron Extensometer clipped onto a coupon. The 3D printed part can be seen on the extensometer in orange.

The tensile tests were performed using a crosshead speed of 5 mm/min. The obtained results were the Young's Modulus, the yield strength (obtained with the 0.2 % rule), the ultimate tensile strength, the maximum elongation and the fracture strength.

3.5.6 Microhardness Testing

The microhardness testing was done using a Struers Duramin (fig. 3.7) with a Vickers indenter tip. 5 indentations were performed on the polished surface of each sample with a load of 19.614 N for a duration of 20 seconds. Only one coupon from each combination of parameters was tested plus as-built coupons P4 and P5.

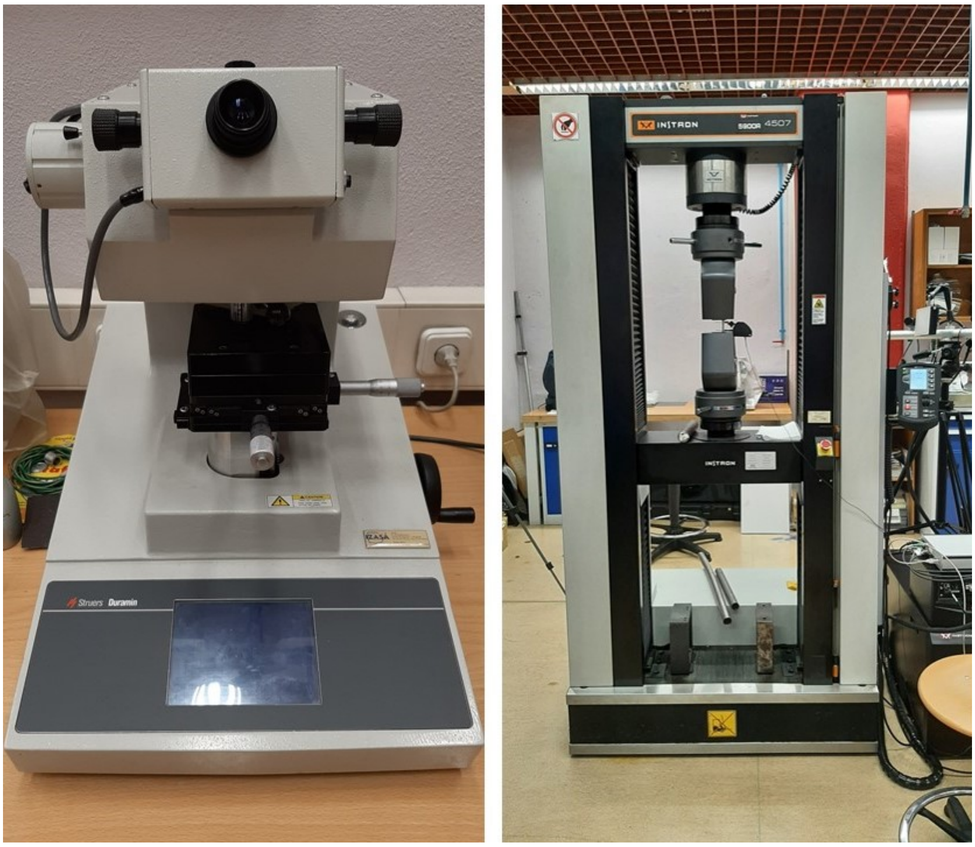

Figure 3.7: Left Image: The Struers Duramin used to perform the microhardness tests. Right Image: The Instron 4507 used to run the tensile tests.

Chapter 4

Results and Discussion

The main focus of this dissertation was to investigate and optimize the heat treatment of Ti-6Al-4V components produced by an L-PBF machine. Since this is being done in the context of medical devices, ideally, the components would have high strength, moderate hardness and ductility as specified in the ASTM F136 standard. This dissertation was also developed as the continuation of another dissertation [54] that studied the effects of the printing parameters on the mechanical properties of Ti-6Al-4V components. The testing results are shown in appendix A.2. The coupons used for this dissertation were printed using the best parameter combination found in that dissertation.

Originally, there had been plans to perform tensile tests on all of the produced coupons. However, due to time constraints and slippage of the coupons during the tensile testing, only 14 of the heat treated samples were successfully tested. All the stress/strain curves can be found in the appendix under appendix B.1.

4.1 As-Built Coupons

In table 4.1, the tensile testing results for the non heat treated samples P4 and P5 are shown. Even though tensile tests were performed on all 5 of the non heat treated coupons, only the full results for the last 2 are shown because of the new extensometer part used. This brought about changes on how the extensometer read the results for the extension and, as a result, some of the non heat treated Ti-6Al-4V coupons as well as some other Steel coupons that were found in the lab were sacrificed in order to verify that the extension readings that were coming from the extensometer were accurate. However, since the stress values were unaffected, the UTS and fracture stress of all samples are shown (for the calculation of the stresses, the initial area of the sample's cross-section was used due to the fact that none of the samples reached the plastic deformation region and thus, the area was remained unchanged throughout).

As for the results, these were not expected. In all 5 tests the coupons averaged a fracture strength of

868.53 ± 72.02 MPa never having reached the yield point. The maximum values for elongation fell just below 1%. The main source for comparison is the aforementioned dissertation [54] where, regardless of the parameters used for the print, the majority of coupons reached the plastic deformation region with a yield strength in the 1030 to 1120 MPa range, an elongation ranging from 2 to 5 % and a UTS of at least 1150 MPa. In the literature, Liu et al. [23] compiled a list of numerous tensile tests performed in various different studies to Ti-6Al-4V coupons with different build orientations and print parameters. The UTS results varied between 1000 and 1450 MPa, yield strengths between 850 and 1300 MPa and elongations between 1.4 and 11.3 %.

Sample No.	**E [GPa]**	**UTS [MPa]**	σ_y **[MPa]**	**Elongation [%]**	σ_f **[MPa]**
P1		765.11	-		765.11
P2		961.38	-		961.38
P3		849.33	-		849.33
P4	119.34	900.97	-	0.84	900.97
P5	95.47	865.86	-	0.90	865.86

Table 4.1: Results obtained from tensile testing done to the non heat treated coupons.

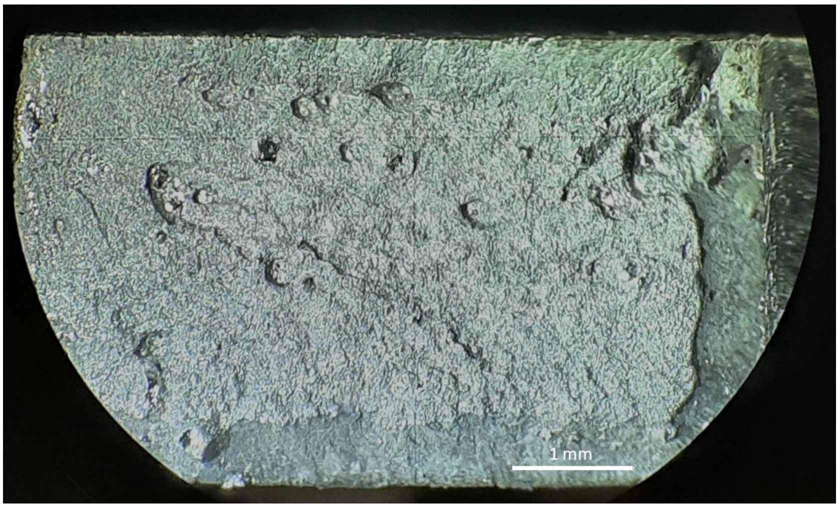

Figure 4.1: Fracture surface of coupon P5.

This data serves to show how inconsistent the mechanical properties of L-PBF produced components can be and how dependent they are of the printing parameters used [55]. Even though this print was performed using the optimized printing parameters obtained in the previous work [54], the fact that the coupons were laid out vertically as opposed to horizontally might have been enough to cause the defects responsible for this mechanical behaviour [12, 13]. Even if all the printing parameters are maintained, changing the orientation of the component on the build plate is known to be enough to cause noticeable differences in mechanical performance [26]. In all of these studies mentioned previously, the non heat treated coupons still reached the plastic deformation region regardless of being machined or not. This evidences the fact that there is something inherently wrong with the machined as-built coupons used as the baseline. It is worth noting that even some articles refer the need to re-print some samples due to poor mechanical performance as exemplified by Vilaro et al. in their article [26].

In figure 4.1 the fracture surface is represented. Porosity is very visible throughout the surface. The round pores are too large to be identified as gas pores (200 μm) but some lack of fusion can be identified in the right side of the fracture, where bright pores with irregular shapes can be seen. In this image it's not very clear, but with the naked eye a more ductile fracture can be seen from the border up to a depth of 0.5 mm, the rest being fragile.

The L-PBF production method is known to produce components with many flaws and defects such as the ones described in section 2.2.3. As the data on table 4.5 shows, the mechanical properties were definitely improved by the heat treatments, in certain cases. This allows for narrowing down which of these defects might be causing the problems. The defects that are most likely to be corrected during the heat treatment processes are the lack of fusion, the residual stresses and the poor microstructure. This means that all other defects (anisotropy, gas pores, balling, hot tears and fish scales) will still be present in the final parts inevitably affecting the mechanical performance. Unfortunately, due to lack of time, a more in-depth investigation exploring the full extent of these defects is not possible.

4.2 Heat Treated Coupons

In this section, the tensile results of the heat treated coupons will be presented, discussed and compared to the as-built coupons from the previous section and the previous work [54] in order to determine how effective they were at improving their properties. An overall literature comparison is done in section 4.2.4.

4.2.1 Sitting Temperature - 800 °C

Looking at the coupons heat treated at 800 °C, they all reach values of UTS between 1130 and 1200 MPa. However, those that were treated for 0.5 h present strain values up to 6 %. The ones treated for 3 h reached 8.22 % (furnace cooled) and 9.61 % (water quenched). Interestingly, the specimen that has the highest fracture strain also has the lowest yield stress of coupons that reached the plastic region. The yield stresses covered a wide range from 850 to 1100 MPa. Just like the yield stresses, the elasticity moduli values covered a wide range (90-127 GPa), which is generally not expected and is certainly a result of the defects still present in the specimens.

It seems like the temperature at which the coupons were treated was the main impacting factor of the UTS as it was the only common factor among the parts. After that, the resting time played the major role in affecting the elongation values as they increased for higher times. This is consistent with the fact that the low ductility microstructure found in as-built parts, α'-phase martensite, starts to decompose into more favorable α + β phases at around 800 °C. [56] The longer sitting times allow for a greater amount of the previous microstructure to be transformed, and thus improve its ductile properties while maintaining the UTS. At sub-transus temperatures, the cooling rate is expected to be the factor with less influence in the final properties, as explained in section 2.2.2.

Temp [°C]	Time [h]	Cooling	E [GPa]	UTS [MPa]	σ_y [MPa]	Strain [%]	σ_f [MPa]
800	**0.5**	**WQ**	105.96	1135.36	912	4.71	1135.09
		OQ + AC	126.63	1130.21	990	5.88	1126.32
		FC	108.29	1191.98	1075	5.94	1191.38
	3	**WQ**	90.65	1150.03	851	9.61	1146.4
		FC	104.33	1164.82	1055	8.22	1160.21

Table 4.2: Tensile testing results for the coupons heat treated at 800 °C.

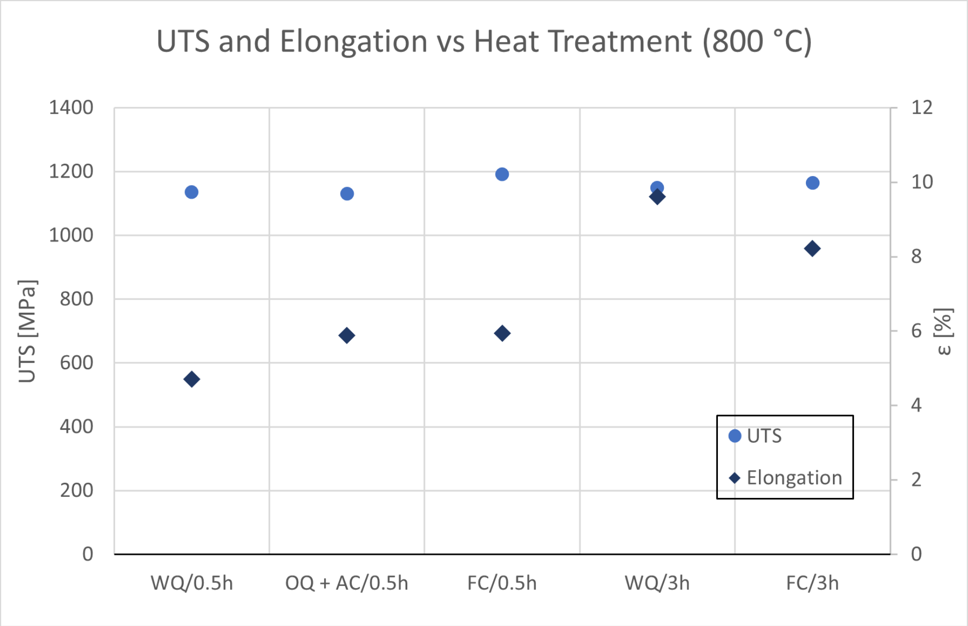

Figure 4.2: Graphical representation of the UTS and the elongation according to the applied heat treatment, more specifically, at the sitting temperature of 800 °C.

This is a great improvement over the as-built coupons since all of these fractured in the plastic region. When comparing to the previous work, the values for UTS are similar (1130-1200 MPa vs 1150-1250 MPa) which is better than what was expected because as-built parts tend to have higher UTS values than their heat treated counterparts. The higher strain values (up from 2-5 %) were an expected result.

4.2.2 Sitting Temperature - 950 °C

At this temperature there's a general decline of the mechanical properties when compared to the coupons treated at 800 °C. As seen in table 4.3 and figure 4.3, half of the 4 coupons didn't reach the phase of plastic deformation. Those that did, reached UTS values of 1100 and 1000 MPa and yield stresses of 911 and 930 MPa. However, the strain values were very low, at about 2.5 %.

The results obtained go completely against the literature. According to Su et al. [35] where they perform very similar heat treatments, the coupons treated at 950 °C perform at a similar range as the coupons treated at 850 °C: UTS $>$ 1000 MPa, YS $>$ 900 MPa and $\varepsilon > 8$ %. While the parts treated for 30 minutes have UTS and YS values that fall within the target range, these still have very low fracture strain results. The other samples don't even reach the plastic region. The only explanation for these sub-par results may come the abnormal defects obtained during manufacturing.

Temp [°C]	**Time [h]**	**Cooling**	**E [GPa]**	**UTS [MPa]**	σ_y **[MPa]**	**Strain [%]**	σ_f **[MPa]**
950	**0.5**	**WQ**	88.37	1107.21	911	2.57	1106.33
		FC	119.26	998.79	930	2.34	992.8
	3	**OQ + AC**	90.48	716.83	-	0.86	716.33
	5	**FC**	98.12	695.77	-	0.89	693.09

Table 4.3: Tensile testing results for the coupons heat treated at 950 °C.

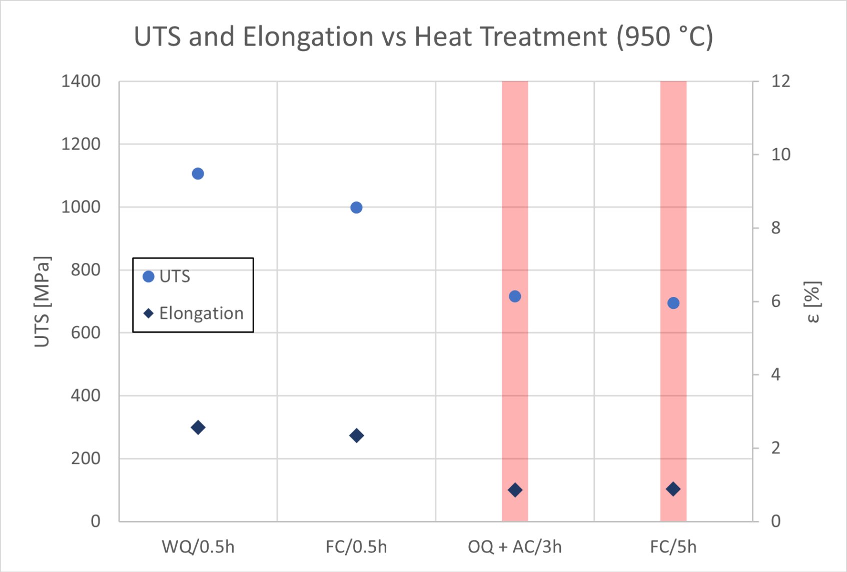

Figure 4.3: Graphical representation of the UTS and the elongation according to the applied heat treatment, more specifically, at the sitting temperature of 950 °C. The vertical red lines indicate the coupons that fractured prior to reaching the elastic region.

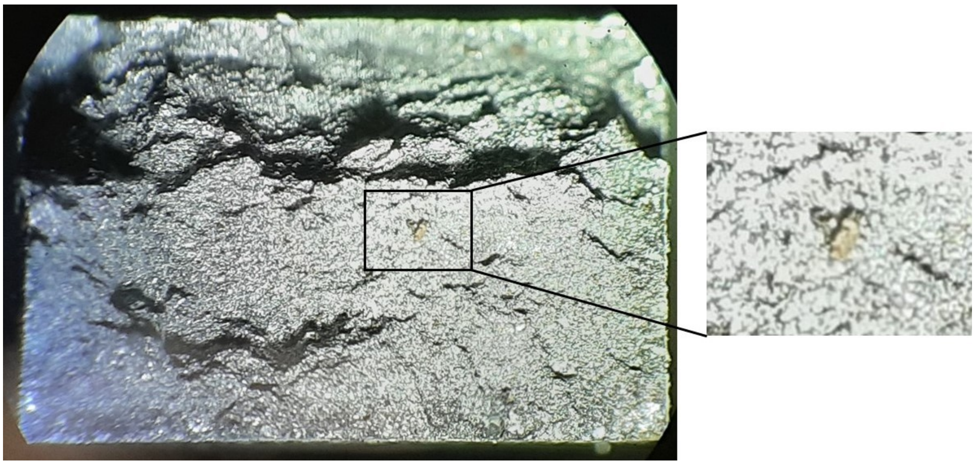

Figure 4.4: Fracture surface of coupon 15 with a zoomed in area showing a brown spot, which is unexpected in this material.

In figure 4.4 the fracture surface of coupon 15 is shown. Data for this coupon was not used for the discussion because it slipped twice during the tensile test and the results were not feasible. However, it could be observed that it fractured in the plastic region. There are some differences when compared to P5, namely that the outer area no longer appears to be of ductile nature. Another topic of interest is that there is a brown spot in the center region of the fracture (highlighted in the figure), the source of which is unidentified.

When comparing to the previous work's results, these cannot be seen as an improvement as the UTS ends up being slightly lower than that of the as-built parts while having the same fracture strain values as the worst ones.

4.2.3 Sitting Temperature - 1100 °C

At this sitting temperature, all the coupons fractured before reaching the plastic deformation region. The main takeaway of these tests is the consistent value of the Young's modulus of the parts cooled in the furnace ranging from 105 to 114 GPa. The registered Young's modulus for the oil quenched sample is certainly an outlier given that this value shouldn't be able to deviate this much from the as-built parts.

Temp. [°C]	Time [h]	Cooling	E [GPa]	UTS [MPa]	σ_y [MPa]	Strain [%]	σ_f [MPa]
1100	**0.5**	**WQ**	94.84	645.49	-	0.68	645.49
		OQ	65.13	422.62	-	0.66	422.62
		FC	113.9	686.12	-	0.74	685.78
	3	**FC**	104.94	328.2	-	0.3	328.2
	5	**FC**	109.79	342.5	-	0.32	342.5

Table 4.4: Tensile testing results for the coupons heat treated at 1100 °C.

Even with only 5 tests at this temperature and the fact they fractured early, some conclusions can be taken. The first three samples show that water quenching and furnace cooling yield similar and greater UTS values over oil quenching. The same is not necessarily observed at lower temperatures, like at 800 °C. Also, from the three samples which were furnace cooled, the most ductile coupon was the one treated for the shortest amount of time. However, the conclusions taken from the specimens that fractured early **may not be trustworthy due to variance caused by the defects**.

One factor that may have exacerbated the weaknesses of these coupons is the fact that the columnar prior-β grains have been erased from the microstructure. Grain morphology can only be altered at super-transus temperatures ($>$ 1000 °C) but there have been reports of prior-β grains shearing at 950 °C [35]. Treating at these temperatures results in a mix of α and β phases or a new α' phase within the newly formed equiaxed grains. This depends on the cooling rate being that the higher it is, the more it tends to the latter microstructure. This newly formed microstructure favors fatigue type loads as opposed to the elongated prior-β grains which favor creep and tensile loads. [26] Compounded with the preexisting defects, this worsened the mechanical properties of the coupons.

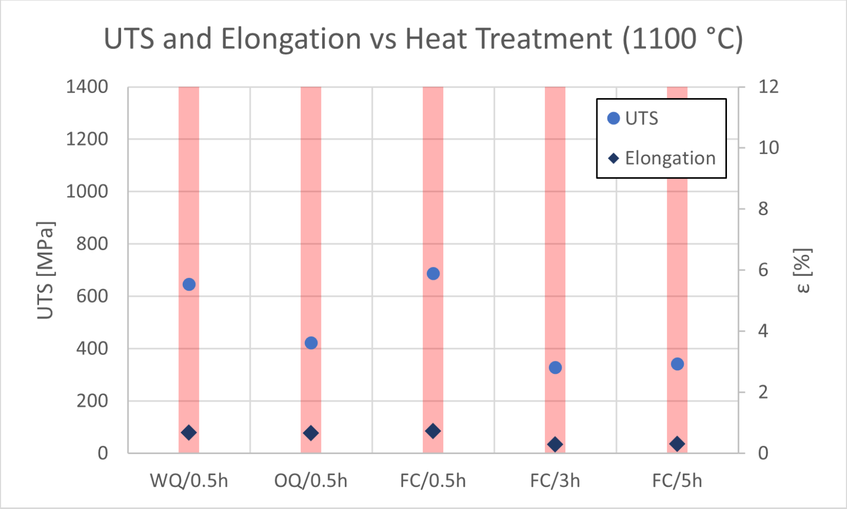

Figure 4.5: Graphical representation of the UTS and the elongation according to the applied heat treatment, more specifically, at the sitting temperature of 1100 °C. The vertical red lines indicate the coupons that fractured prior to reaching the elastic region.

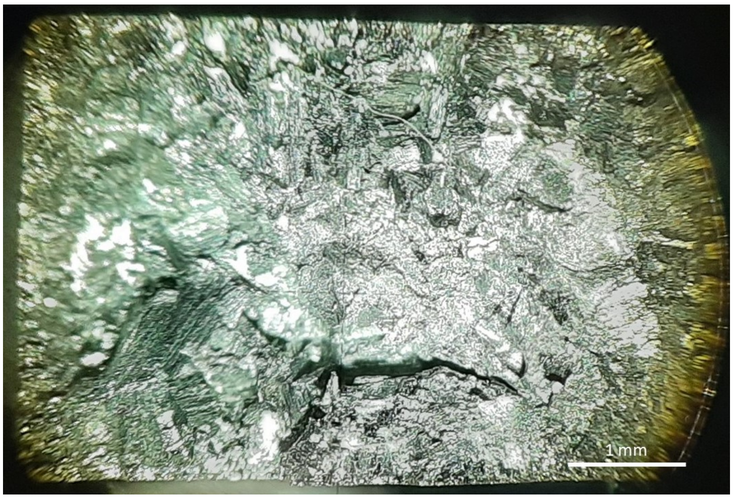

Figure 4.6: Fracture surface of a coupon treated at 1100°C.

In figure 4.6 the fracture surface of a coupon treated at 1100°C is shown. Here the type of fracture is completely different from the previous 2 as it is considerably more brittle. This comes as a result of treating the coupon above the β-transus completely altering the microstructure, as previously mentioned.

4.2.4 Overall Analysis

A full overview of the results can be found in table 4.5 and figure 4.7. From a general perspective, the parts treated at lower temperatures were the ones that performed best as they had less chances of fracturing early. There was also great variability regarding the Young's Modulus. The water quenched samples showed the lowest values, ranging from 88 to 106 GPa, the furnace cooled samples presented results in a more expected range, from 104 to 120 GPa. The highest value was obtained by an oil quenched coupon with 126 GPa. Thermally treated components usually have a Young's modulus up to 10 MPa above or below their as-built counterparts'. [26, 30]

Temp [°C]	Time [h]	Cooling	E [GPa]	UTS [MPa]	σ_y [MPa]	Strain [%]	σ_f [MPa]
800	**0.5**	**WQ**	105.96	1135.36	912	4.71	1135.09
		OQ + AC	126.63	1130.21	990	5.88	1126.32
		FC	108.29	1191.98	1075	5.94	1191.38
	3	**WQ**	90.65	1150.03	851	9.61	1146.40
		FC	104.33	1164.82	1055	8.22	1160.21
950	**0.5**	**WQ**	88.37	1107.21	911	2.57	1106.33
		FC	119.26	998.79	930	2.34	992.80
	3	**OQ + AC**	90.48	716.83	-	0.86	716.33
	5	**FC**	98.12	695.77	-	0.89	693.09
1100	**0.5**	**WQ**	94.84	645.49	-	0.68	645.49
		OQ	65.13	422.62	-	0.66	422.62
		FC	113.9	686.12	-	0.74	685.78
	3	**FC**	104.94	328.20	-	0.30	328.20
	5	**FC**	109.79	342.50	-	0.32	342.50

Table 4.5: Tensile testing results of the heat treated coupons.

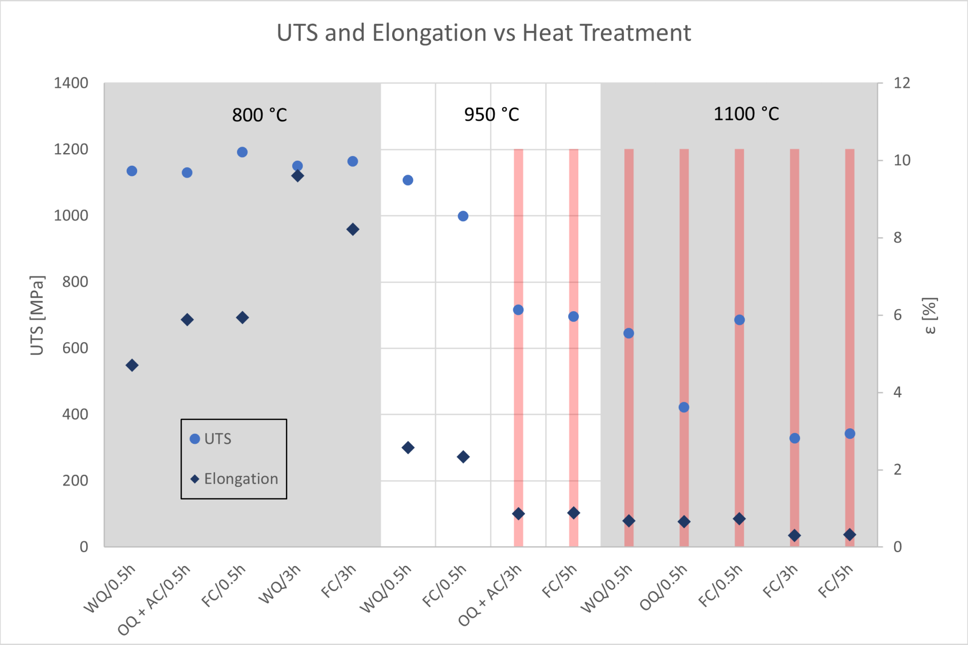

Figure 4.7: Graphical representation of the UTS and the elongation according to the applied heat treatment, more specifically, the sitting temperature. The vertical red lines indicate the coupons that fractured prior to reaching the elastic region.

In a study performed by Su et al. [35], they compare the results from heat treating SLMed coupons at 850 °C, 950 °C and 1100 °C (all for 2h) and cooling them down by water quenching, air cooling and furnace cooling. The results obtained were mostly similar (except for the 950 °C treated ones) to those obtained here. The coupons heated at 1100 °C had varying UTS and YS values but the lowest strain (about 2%) confirming the high brittleness of these specimens and the reason why all of the ones tested here fractured in the elastic region. It's also worth noting that, just like for the water quenched samples, except for the 850 °C one, exhibited the most brittle characteristics (high UTS and YS, and low strain) in their temperatures. This leads to their final conclusion. The authors claim that the 850 °C + WQ sample resulted in the better combination of mechanical properties, which is in line with the sample with the best mechanical properties (800 °C/3h/WQ). They claim that, upon analyzing the microstructure, the α' phase was transformed into stable α phase while retaining, to a certain extent, the fine and hierarchical grain structure present in as-built parts as seen in figure 4.8. This allowed for a notable increase in fracture strain in exchange for a slight decrease in UTS and YS.

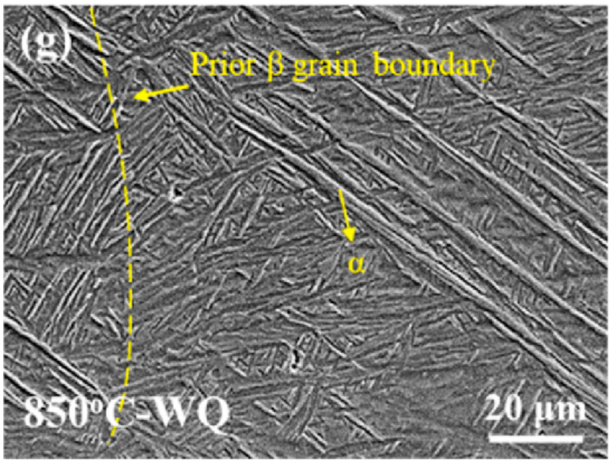

Figure 4.8: Microstructure of an SLMed sample after being heat treated at 850°C for 2h and being water quenched. [35]

According to Mur et. al, the acicular α' microstructure present in as-built parts, which is responsible for their more fragile behavior, is completely decomposed when heat treated at temperatures starting at 800 °C. This is, once again, replaced with the more stable phases α + β. [56] Heat treating at this temperature is also enough to rid the parts of all residual stresses resulting in better mechanical performance. [57] While the second factor is applied to all the heat treated parts, the final microstructure of the part is heavily dependent on all three heat treating parameters depending on whether they were treated at sub-transus or super-transus temperatures, as explained in section 2.2.2. In the end, the most favorable sitting temperature for these coupons was 800 °C, which is one of the most important parameters at sub-transus temperatures. It resulted in the best microstructure, akin to what the previously mentioned study ([35]) reported and presented in figure 4.8.

Microhardness Testing

For these tests, 5 indentations were performed on the polished surface of each sample with a load of 19.614 N for a duration of 20 seconds. Only one coupon from each combination of parameters was tested plus as-built coupons P4 and P5. The following tables show the results obtained from the hardness testing. Tables 4.6 and 4.7 show the results from the heat treated and the as-built samples respectively. Table 4.8 shows the average hardness for coupons grouped by an isolated parameter. The detailed values can be found in the appendix under section B.2

The values obtained for the as-built specimens resulted in an average of 433.4 HV, which is high considering the values obtained in the previous dissertation [54] done on the topic (ranging from 350 to 400 HV) but within the expected range found in the literature which specifies values spanning from 300 to 500 HV. [58, 59]

Time [h]	**Cooling**	**Temperature [°C]**		
		800	**950**	**1100**
0.5	**WQ**	370.8	409.2	477.8
	OQ	403	499.6	498.8
	OQ + AC	389.8	426.4	529.4
	FC	391.4	415.6	464
3	**WQ**	366	527.2	583
	OQ	391.8	510.8	623
	OQ + AC	434	439.4	636.2
	FC	373	578	459
5	**WQ**	464	522.8	581.2
	OQ	379.8	499.8	609
	OQ + AC	450	545.6	671.4
	FC	442.4	488.6	495

Table 4.6: Surface microhardness [HV] values obtained for the heat treated components.

P4	437.2
P5	429.6
Avg.	433.4

Table 4.7: Surface microhardness [HV] values obtained for the as-built parts.

Temperature [°C]		**Time [h]**		**Cooling Method**	
800	404.67	**0.5**	439.65	**FC**	456.33
950	488.58	**3**	493.45	**WQ**	478
1100	552.32	**5**	512.47	**OQ**	490.62
				OQ + AC	502.47

Table 4.8: Average microhardness [HV] values for coupons treated with a certain parameter.

As for the heat treated results, the obtained values ranged from 366 to 671.4 HV. There is a clear correlation between the sitting temperature and the hardness of the specimens. Each average value is separated by roughly 80 HV showing that increasing the temperature results is harder components. The same tendencies can be observed, although to a lesser extent, with the other parameters. Higher resting times also lead to higher hardness values. The different cooling methods only resulted in a maximum difference of 50 HV from the lowest and highest averages. Had there been the possibility of testing components that had only been air cooled, it is likely that these would have fallen in between water quenching and furnace cooling as air cooling produces an intermediate cooling rate between the other two methods. The fact that it didn't happen with the OQ + AC coupons shows the relevance of knowing the conditions of the part prior to performing any sort of post processing.

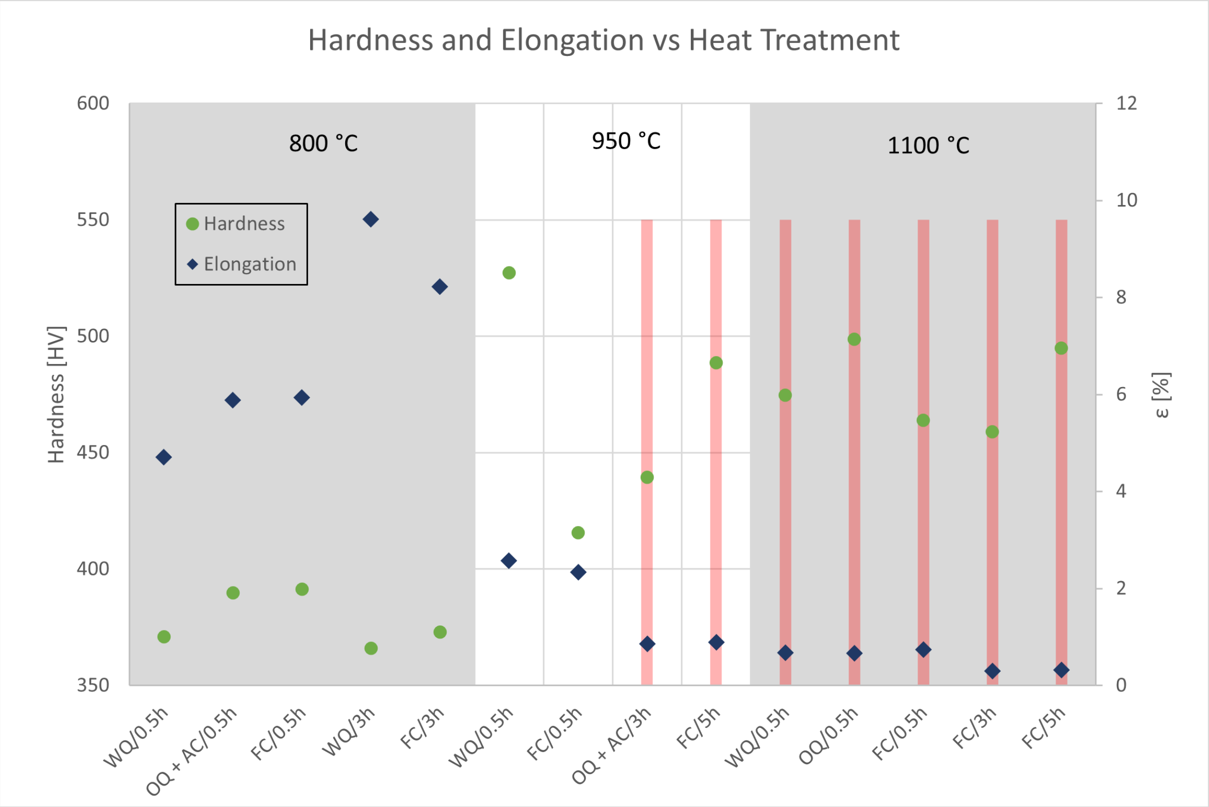

Figure 4.9: Graphical representation of the hardness and the elongation according to the applied heat treatment, more specifically, the sitting temperature. The vertical red lines indicate the coupons that fractured prior to reaching the elastic region.

Figure 4.9 shows the relation between the hardness values and the strain fracture values of the tensile tested specimens. This shows an inverse relation between the values, which was to be expected. The higher the strain, the lower the hardness tends to be (the 950ºC/WQ/3h coupon is an outlier in this case). It is also worth noting that the coupon designated to be the best due to its tensile properties registered the lowest hardness out of all tests, with a hardness value of 366 HV.

Chapter 5

Conclusions

The possibility of producing components through L-PBF is of utmost importance as it allows for complex structures to be created with very little wasted material and less machining. However, the full mechanical potential of these parts remains untapped as they can be further improved. This dissertation sought to find the best way of optimizing the mechanical properties of these components through the use of traditional heat treating after their production.

These were the conclusions retained from studying the three parameters (resting time, resting temperature and cooling method) of these heat treatments:

- The results obtained emphasize the difficulty in replicating the same results in L-PBF when there is not quality control of every aspect of the printing process, like the powder. This had consequences in the results of the heat treated samples with many fracturing before reaching the plastic region.
- The used powder is one of those aspects and a possible cause for the lackluster results. The information provided by the manufacturer may not be exactly accurate depending on the lot and may yield unpredictable results.
- When performing a first time print of a component, it is always imperative to carefully pick the print parameters in accordance with what is being printed. In this case, coupons were printed vertically with printing parameters that had been optimized for horizontal printing. This is believed to be the reason why most samples underperformed mechanically.
- In addition to the previous point, printing components in layers perpendicular to the direction of the main applied force will generally result in worse mechanical properties as the fracture mechanisms will be different. [13]
- High cooling rates in Ti-6Al-4V components are known to result in an α' martensitic microstructure which turns them brittle. However, when performed after a heat treatment, the lower the sitting temperature, the lower its influence becomes and actually becoming beneficial at a certain point by maintaining a balance of fine grain size and favorable phases.

- The heat treating parameter that affects hardness the most is the resting temperature. The higher it is, the higher the material's hardness will be.

Considering all the identified problems, the fact that the orientation of the coupons was unfavorable both due to non optimized print parameters and bad loading direction, the combination of heat treating parameters that ended up yielding the component with the most favorable assortment of mechanical properties while correcting these issues was the following:

Sitting Temperature [ºC]	**Sitting Time [h]**	**Cooling Method**
800	3	Water Quenching

Table 5.1: Heat treating parameters that yielded the best results.

5.1 Future Work

There is still some work that could be done to complement the results of this thesis. The rest of the samples could be submitted to tensile and interior microhardness tests. Furthermore, analysing the fractures with the aid of a SEM or using a μCT to analyze the coupons and identifying the source of the lackluster mechanical properties would bring great insight into what might have gone wrong during the production of the components. Lastly, analysing the microstructure of some samples could also bring more knowledge regarding their potential mechanical properties.

Aside from the analysis that can be done on the existing coupons, what's left is to ascertain the quality of the powder as we can only rely on the information given by the provider. This can be done by reprinting the coupons in all orientations: horizontally along the flat and narrow edges and vertically within the same print and maintaining the same conditions.

As for what's next, a better look into hipping could be of interest as it has been shown to keep the tensile properties obtained through conventional HT as well as significantly improving fatigue properties through its characteristic reduction of porosity. Performing L-PBF in a vacuum environment, although not necessary, has also shown some improvements over conventional L-PBF manufacturing and could bring a new level of optimization as gas entrapment would no longer occur. Lastly, further exploring combinations of consecutive heat treatments could prove to reveal ways of reaching new combinations of mechanical properties.

Bibliography

[1] What is 3d printing? - technology definition and types. URL `https://www.twi-global.com/technical-knowledge/faqs/what-is-3d-printing`.

[2] C. Y. Yap, C. K. Chua, Z. L. Dong, Z. H. Liu, D. Q. Zhang, L. E. Loh, and S. L. Sing. Review of selective laser melting: Materials and applications. *Applied Physics Reviews*, 2(4):041101, 2015. doi: 10.1063/1.4935926.

[3] C. S. Rakesh, N. Priyanka, R. Jayaganthan, and N. J. Vasa. Effect of build atmosphere on the mechanical properties of alsi10mg produced by selective laser melting. *Materials Today: Proceedings*, 5(9):17231–17238, 2018. doi: 10.1016/j.matpr.2018.04.133.

[4] H. Lee, C. H. J. Lim, M. J. Low, N. Tham, V. M. Murukeshan, and Y.-J. Kim. Lasers in additive manufacturing: A review. *International Journal of Precision Engineering and Manufacturing-Green Technology*, 4(3):307–322, 2017. doi: 10.1007/s40684-017-0037-7.

[5] A. F. D. Souza, K. S. Al-Rubaie, S. Marques, B. Zluhan, and E. C. Santos. Effect of laser speed, layer thickness, and part position on the mechanical properties of maraging 300 parts manufactured by selective laser melting. *Materials Science and Engineering: A*, 767:138425, 2019. doi: 10.1016/j.msea.2019.138425.

[6] Q. Nguyen, D. Luu, S. Nai, Z. Zhu, Z. Chen, and J. Wei. The role of powder layer thickness on the quality of slm printed parts. *Archives of Civil and Mechanical Engineering*, 18(3):948–955, 2018. doi: 10.1016/j.acme.2018.01.015.

[7] B. Dutta and F. H. Froes. *Additive Manufacturing of Titanium Alloys*. Elsevier, 2016.

[8] H. Ali, H. Ghadbeigi, and K. Mumtaz. Effect of scanning strategies on residual stress and mechanical properties of selective laser melted ti6al4v. *Materials Science and Engineering: A*, 712: 175–187, 2018. doi: 10.1016/j.msea.2017.11.103.

[9] J. H. Tan, W. L. E. Wong, and K. W. Dalgarno. An overview of powder granulometry on feedstock and part performance in the selective laser melting process. *Additive Manufacturing*, 18:228–255, 2017. doi: 10.1016/j.addma.2017.10.011.

[10] T. Majumdar, T. Bazin, E. M. C. Ribeiro, J. E. Frith, and N. Birbilis. Understanding the effects

of pbf process parameter interplay on ti-6al-4v surface properties. *Plos One*, 14(8), 2019. doi: 10.1371/journal.pone.0221198.

[11] S. E. Brika and V. Brailovski. Influence of powder particle morphology on the static and fatigue properties of laser powder bed-fused ti-6al-4v components. *Journal of Manufacturing and Materials Processing*, 4(4):107, 2020. doi: 10.3390/jmmp4040107.

[12] P. Hartunian and M. Eshraghi. Effect of build orientation on the microstructure and mechanical properties of selective laser-melted ti-6al-4v alloy. *Journal of Manufacturing and Materials Processing*, 2(4):69, 2018. doi: 10.3390/jmmp2040069.

[13] M. Simonelli, Y. Tse, and C. Tuck. Effect of the build orientation on the mechanical properties and fracture modes of slm ti–6al–4v. *Materials Science and Engineering: A*, 616:1–11, 2014. doi: 10.1016/j.msea.2014.07.086.

[14] Z. Xie, Y. Dai, X. Ou, S. Ni, and M. Song. Effects of selective laser melting build orientations on the microstructure and tensile performance of ti–6al–4v alloy. *Materials Science and Engineering: A*, 776:139001, 2020. doi: 10.1016/j.msea.2020.139001.

[15] C. Cepeda-Jiménez, F. Potenza, E. Magalini, V. Luchin, A. Molinari, and M. Pérez-Prado. Effect of energy density on the microstructure and texture evolution of ti-6al-4v manufactured by laser powder bed fusion. *Materials Characterization*, 163:110238, 2020. doi: 10.1016/j.matchar.2020.110238.

[16] Effect of printing conditions on porosity formation in powder bed melting of ti-6al-4v parts : An approach based on 3d x-ray tomography. *SAMT SUDOE*. URL `https://www.samtsudoe.com/wp-content/uploads/2019/09/White-paper1-EN.pdf`.

[17] D. Herzog, V. Seyda, E. Wycisk, and C. Emmelmann. Additive manufacturing of metals. *Acta Materialia*, 117:371–392, 2016. doi: 10.1016/j.actamat.2016.07.019.

[18] H. Gong, K. Rafi, H. Gu, T. Starr, and B. Stucker. Analysis of defect generation in ti–6al–4v parts made using powder bed fusion additive manufacturing processes. *Additive Manufacturing*, 1-4: 87–98, 2014. doi: 10.1016/j.addma.2014.08.002.

[19] W. Sha and S. Malinov. *Titanium alloys: modelling of microstructure, properties and applications*. Woodhead Publishing Limited, 2009.

[20] *ASM handbook volume 9: metallography and microstructures*. ASM International, 2004.

[21] J. Sieniawski, W. Ziaja, K. Kubiak, and M. Motyk. Microstructure and mechanical properties of high strength two-phase titanium alloys. *Titanium Alloys - Advances in Properties Control*, 2013. doi: 10.5772/56197.

[22] Y. Xu, Y. Lu, J. Liang, and R. D. Sisson. Microstructure and corrosion behaviour of additively manufactured ti–6al–4v with various post-heat treatments. *Materials Science and Technology*, 35 (1):89–97, 2018. doi: 10.1080/02670836.2018.1542052.

[23] S. Liu and Y. C. Shin. Additive manufacturing of ti6al4v alloy: A review. *Materials and Design*, 164: 107552, 2019. doi: 10.1016/j.matdes.2018.107552.

[24] L. Thijs, F. Verhaeghe, T. Craeghs, J. V. Humbeeck, and J.-P. Kruth. A study of the microstructural evolution during selective laser melting of ti–6al–4v. *Acta Materialia*, 58(9):3303–3312, 2010. doi: 10.1016/j.actamat.2010.02.004.

[25] L. Murr, S. Quinones, S. Gaytan, M. Lopez, A. Rodela, E. Martinez, D. Hernandez, E. Martinez, F. Medina, R. Wicker, and et al. Microstructure and mechanical behavior of ti–6al–4v produced by rapid-layer manufacturing, for biomedical applications. *Journal of the Mechanical Behavior of Biomedical Materials*, 2(1):20–32, 2009. doi: 10.1016/j.jmbbm.2008.05.004.

[26] T. Vilaro, C. Colin, and J. D. Bartout. As-fabricated and heat-treated microstructures of the ti-6al-4v alloy processed by selective laser melting. *Metallurgical and Materials Transactions A*, 42(10): 3190–3199, 2011. doi: 10.1007/s11661-011-0731-y.

[27] R. Boyer, E. W. Collings, and G. Welsch. *Materials properties handbook: titanium alloys*. ASM International, 2007.

[28] A. Polishetty, G. Littlefair, and K. P. Kumar. Machinability assessment of titanium alloy ti-6al-4v for biomedical applications. *Advanced Materials Research*, 941-944:1985–1990, 2014. doi: 10.4028/www.scientific.net/amr.941-944.1985.

[29] A. Ducato, L. Fratini, M. La Cascia, and G. Mazzola. An automated visual inspection system for the classification of the phases of ti-6al-4v titanium alloy. pages 362–369, 08 2013. doi: 10.1007/978-3-642-40246-3_45.

[30] B. Vrancken, L. Thijs, J.-P. Kruth, and J. V. Humbeeck. Heat treatment of ti6al4v produced by selective laser melting: Microstructure and mechanical properties. *Journal of Alloys and Compounds*, 541:177–185, 2012. doi: 10.1016/j.jallcom.2012.07.022.

[31] H. V. Atkinson and S. Davies. Fundamental aspects of hot isostatic pressing: An overview. *Metallurgical and Materials Transactions A*, 31(12):2981–3000, 2000. doi: 10.1007/s11661-000-0078-2.

[32] M. H. Bocanegra-Bernal. Hot isostatic pressing (hip) technology and its applications to metals and ceramics. *Journal of Materials Science*, 39(21):6399–6420, 2004. doi: 10.1023/b:jmsc.0000044878.11441.90.

[33] X. Huang, L. Lang, S. Gong, and M. Zhao. Effect of post-treatment on the microstructure and mechanical properties of selective laser melted ti6al4v lattice structures. *Rapid Prototyping Journal*, 26(9):1569–1577, 2020. doi: 10.1108/rpj-11-2019-0284.

[34] P. Jamshidi, M. Aristizabal, W. Kong, V. Villapun, S. C. Cox, L. M. Grover, and M. M. Attallah. Selective laser melting of ti-6al-4v: The impact of post-processing on the tensile, fatigue and biological properties for medical implant applications. *Materials*, 13(12):2813, 2020. doi: 10.3390/ma13122813.

[35] C. Su, H. Yu, Z. Wang, J. Yang, and X. Zeng. Controlling the tensile and fatigue properties of selective laser melted ti–6al–4v alloy by post treatment. *Journal of Alloys and Compounds*, 857: 157552, 2021. doi: 10.1016/j.jallcom.2020.157552.

[36] X. Zhao, S. Li, M. Zhang, Y. Liu, T. B. Sercombe, S. Wang, Y. Hao, R. Yang, and L. E. Murr. Comparison of the microstructures and mechanical properties of ti–6al–4v fabricated by selective laser melting and electron beam melting. *Materials & Design*, 95:21–31, 2016. doi: 10.1016/j.matdes.2015.12.135.

[37] P.-W. Lui, C.-M. Chang, H.-H. Wang, Y.-P. Lin, and F.-M. Lai. Mechanical properties of porous ti-6al-4v alloys prepared by selective laser melting and post-heat treatments. *Sensors and Materials*, 31(11):3629, 2019. doi: 10.18494/sam.2019.2507.

[38] F. Dominique, A. Pineau, and A. Zaoui. *Comportement mécanique des matériaux*. Hermès, 2009.

[39] H. Yu, F. Li, Z. Wang, and X. Zeng. Fatigue performances of selective laser melted ti-6al-4v alloy: Influence of surface finishing, hot isostatic pressing and heat treatments. *International Journal of Fatigue*, 120:175–183, 2019. doi: 10.1016/j.ijfatigue.2018.11.019.

[40] Z. Chen, S. Cao, X. Wu, and C. H. Davies. Surface roughness and fatigue properties of selective laser melted ti–6al–4v alloy. *Additive Manufacturing for the Aerospace Industry*, page 283–299, 2019. doi: 10.1016/b978-0-12-814062-8.00015-7.

[41] G. Qian, Z. Jian, X. Pan, and F. Berto. In-situ investigation on fatigue behaviors of ti-6al-4v manufactured by selective laser melting. *International Journal of Fatigue*, 133:105424, 2020. doi: 10.1016/j.ijfatigue.2019.105424.

[42] A. Fatemi, R. Molaei, J. Simsiriwong, N. Sanaei, J. Pegues, B. Torries, N. Phan, and N. Shamsaei. Fatigue behaviour of additive manufactured materials: An overview of some recent experimental studies on ti-6al-4v considering various processing and loading direction effects. *Fatigue & Fracture of Engineering Materials & Structures*, 42(5):991–1009, 2019. doi: 10.1111/ffe.13000.

[43] J.-M. Oh, K.-H. Heo, W.-B. Kim, G.-S. Choi, and J.-W. Lim. Sintering properties of ti-6al-4v alloys prepared using ti/tih$_2$ powders. *MATERIALS TRANSACTIONS*, advpub, 2013. doi: 10.2320/matertrans.M2012304.

[44] B. Zhou, J. Zhou, H. Li, and F. Lin. A study of the microstructures and mechanical properties of ti6al4v fabricated by slm under vacuum. *Materials Science and Engineering: A*, 724:1–10, 2018. doi: 10.1016/j.msea.2018.03.021.

[45] J. L. Bartlett and X. Li. An overview of residual stresses in metal powder bed fusion. *Additive Manufacturing*, 27:131–149, 2019. doi: 10.1016/j.addma.2019.02.020.

[46] C. Romero, F. Yang, and L. Bolzoni. Fatigue and fracture properties of ti alloys from powder-based processes – a review. *International Journal of Fatigue*, 117:407–419, 2018. doi: 10.1016/j.ijfatigue.2018.08.029.

[47] J. Kruth. Selective laser melting of iron-based powder. *Journal of Materials Processing Technology*, 2004. doi: 10.1016/s0924-0136(04)00220-1.

[48] M. Agarwala, D. Bourell, J. Beaman, H. Marcus, and J. Barlow. Direct selective laser sintering of metals. *Rapid Prototyping Journal*, 1(1):26–36, 1995. doi: 10.1108/13552549510078113.

[49] H. Shipley, D. Mcdonnell, M. Culleton, R. Coull, R. Lupoi, G. Odonnell, and D. Trimble. Optimisation of process parameters to address fundamental challenges during selective laser melting of ti-6al-4v: A review. *International Journal of Machine Tools and Manufacture*, 128:1–20, 2018. doi: 10.1016/j.ijmachtools.2018.01.003.

[50] S. Bagehorn, J. Wehr, and H. Maier. Application of mechanical surface finishing processes for roughness reduction and fatigue improvement of additively manufactured ti-6al-4v parts. *International Journal of Fatigue*, 102:135–142, 2017. doi: 10.1016/j.ijfatigue.2017.05.008.

[51] A. K. Singla, M. Banerjee, A. Sharma, J. Singh, A. Bansal, M. K. Gupta, N. Khanna, A. Shahi, and D. K. Goyal. Selective laser melting of ti6al4v alloy: Process parameters, defects and post-treatments. *Journal of Manufacturing Processes*, 64:161–187, 2021. doi: 10.1016/j.jmapro.2021.01.009.

[52] P. Collins, D. Brice, P. Samimi, I. Ghamarian, and H. Fraser. Microstructural control of additively manufactured metallic materials. *Annual Review of Materials Research*, 46(1):63–91, 2016. doi: 10.1146/annurev-matsci-070115-031816.

[53] 3T-AM. Titanium ti-6al-4v - data sheet. URL `https://www.3t-am.com/sites/threeT/files/TitaniumTi6Al4V_Datasheet.pdf`.

[54] B. A. B. Ropio. Validation of metal additive manufacturing parts. Master's thesis, Universidade de Lisboa - Instituto Superior Técnico, 2018.

[55] C. K. Chua, C. H. Wong, and W. Y. Yeong. *Standards, quality control, and measurement sciences in 3D printing and additive manufacturing*. Elsevier, Academic Press, 2017.

[56] F. G. Mur, D. Rodríguez, and J. Planell. Influence of tempering temperature and time on the α'-ti-6al-4v martensite. *Journal of Alloys and Compounds*, 234(2):287–289, 1996. doi: 10.1016/0925-8388(95)02057-8.

[57] S. Leuders, M. Thöne, A. Riemer, T. Niendorf, T. Tröster, H. Richard, and H. Maier. On the mechanical behaviour of titanium alloy tial6v4 manufactured by selective laser melting: Fatigue resistance and crack growth performance. *International Journal of Fatigue*, 48:300–307, 2013. doi: 10.1016/j.ijfatigue.2012.11.011.

[58] J. Tong, C. R. Bowen, J. Persson, and A. Plummer. Mechanical properties of titanium-based ti–6al–4v alloys manufactured by powder bed additive manufacture. *Materials Science and Technology*, 33(2):138–148, 2016. doi: 10.1080/02670836.2016.1172787.

[59] A. Leicht and E. O. Wennberg. Analyzing the mechanical behavior of additive manufactured ti 6al 4v using digital image correlation. Master's thesis, CHALMERS UNIVERSITY OF TECHNOLOGY, 2015.

Appendix A

Process Parameters

A.1 Coupon Heat Treatment Parameters

Coupon No.	Resting Temperature [°C]	Resting Time [h]	Cooling Method
1	800	0,5	Water
2			Oil
3			Furnace
4		3	Water
5			Oil
6			Furnace
7		5	Water
8			Oil
9			Furnace
10	950	0,5	Water
11			Oil
12			Furnace
13		3	Water
14			Oil
15			Furnace
16		5	Water
17			Oil
18			Furnace
19	1100	0,5	Water
20			Oil
21			Furnace
22		3	Water
23			Oil
24			Furnace
25		5	Water
26			Oil
27			Furnace
28	800	0,5	Air (after Oil Quenching)
29		3	
30		5	
31	950	0,5	
32		3	
33		5	
34	1100	0,5	
35		3	
36		5	

Table A.1: Detailed list of the different combinations of parameters used to produce the testing coupons.

A.2 Previous Work's Tensile Testing Results

The table below shows the results obtained from Beatriz Ropio's dissertation [54]. Each row represents a set of tests performed to coupons which were produced with a certain set of parameters.

Set	**Young's modulus [GPa]**	**UTS [MPa]**	**Yield strength [MPa]**	**Elongation [%]**
1	108.47 ± 2.29	1222.25 ± 13.82	1072.00 ± 11.79	3.415 ± 0.90
2	119.44 ± 13.46	1220.63 ± 50.40	1111.00 ± 23.30	2.22 ± 0.93
3	110.60 ± 3.31	1238.32 ± 8.72	1097.00 ± 9.02	3.44 ± 0.18
4	108.80 ± 3.94	1220.43 ± 19.43	1063.00 ± 20.01	3.05 ± 0.77
5	108.89 ± 3.61	1200.38 ± 43.07	1073.00 ± 18.50	2.745 ± 0.98
6	105.89 ± 3.24	1206.25 ± 15.31	1037.00 ± 14.19	2.75 ± 0.47
7	111.52 ± 10.55	1189.56 ± 60.48	1056.00 ± 10.12	2.84 ± 1.45
8	112.91 ± 7.56	1220.10 ± 14.81	1086.00 ± 12.50	3.53 ± 0.99
9	116.16 ± 11.29	1246.15 ± 13.40	1078.00 ± 13.53	3.23 ± 0.94
10	105.94 ± 10.26	1220.05 ± 18.52	1073.00 ± 25.94	4.51 ± 1.51
11	111.08 ± 6.89	1224.39 ± 20.48	1076.00 ± 14.93	2.95 ± 0.57
12	113.97 ± 6.91	1151.95 ±143.21	1082.00 ± 3.51	2.94 ± 1.73
13	112.42 ± 10.07	1209.97 ± 15.20	1074.00 ± 20.11	2.69 ± 0.90

Table A.2: Results from the tensile testing performed in the previous work.

Appendix B

Mechanical Testing Results

B.1 Stress vs Strain Plots

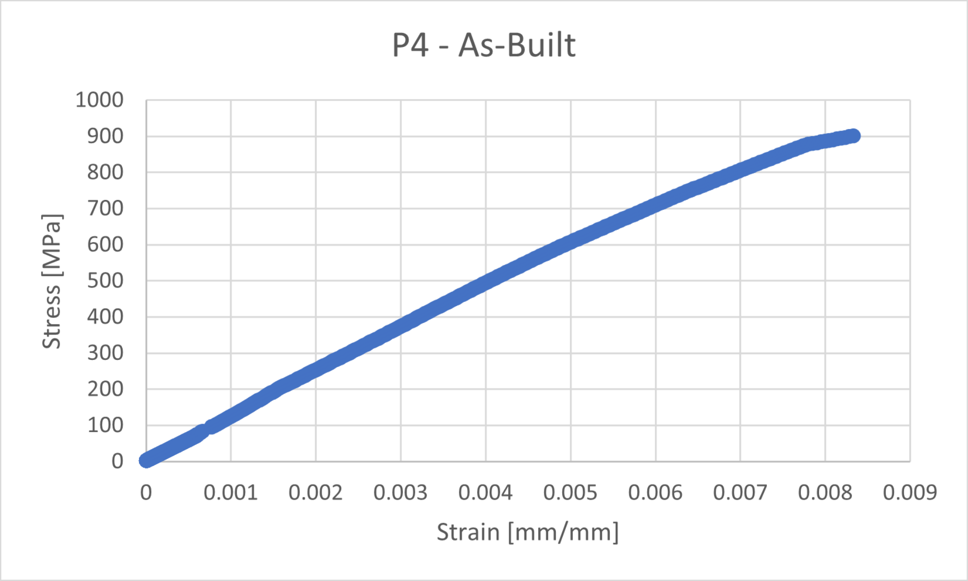

Figure B.1: Stress vs Strain plot for sample number P4.

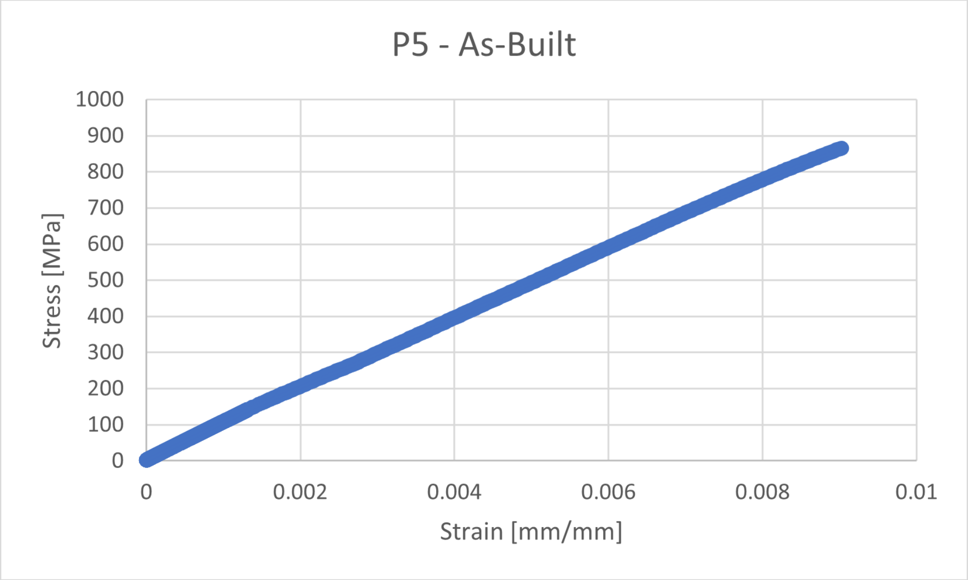

Figure B.2: Stress vs Strain plot for sample number P5.

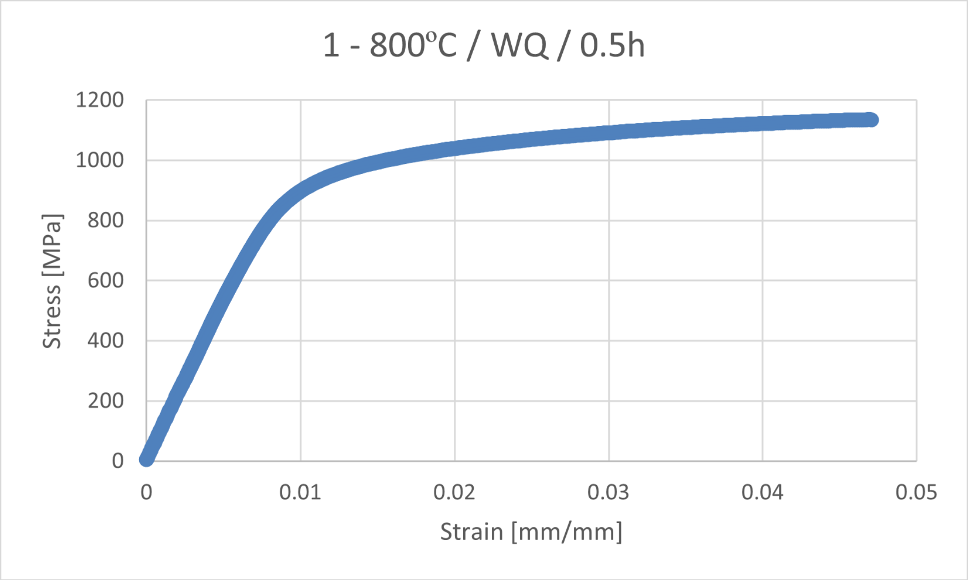

Figure B.3: Stress vs Strain plot for sample number 1.

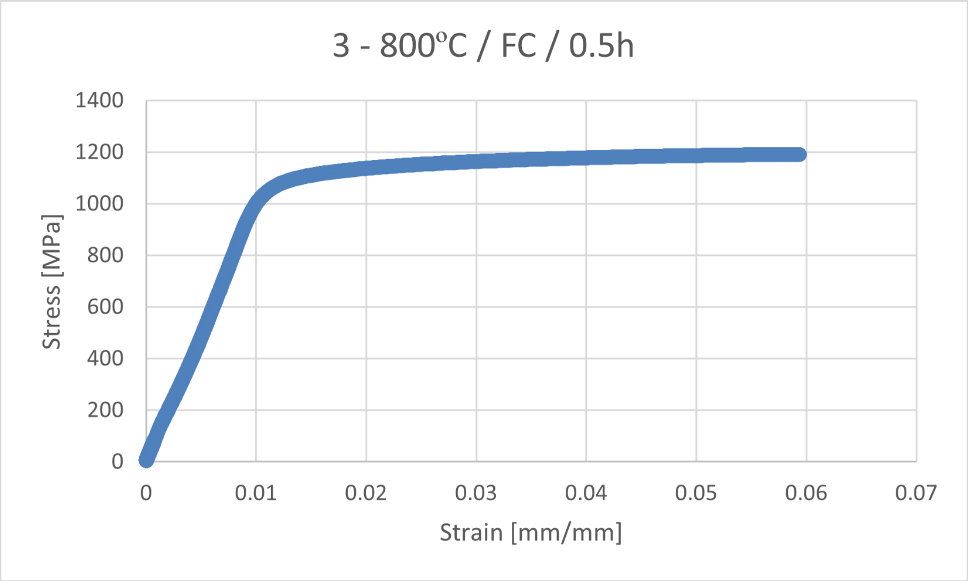

Figure B.4: Stress vs Strain plot for sample number 3.

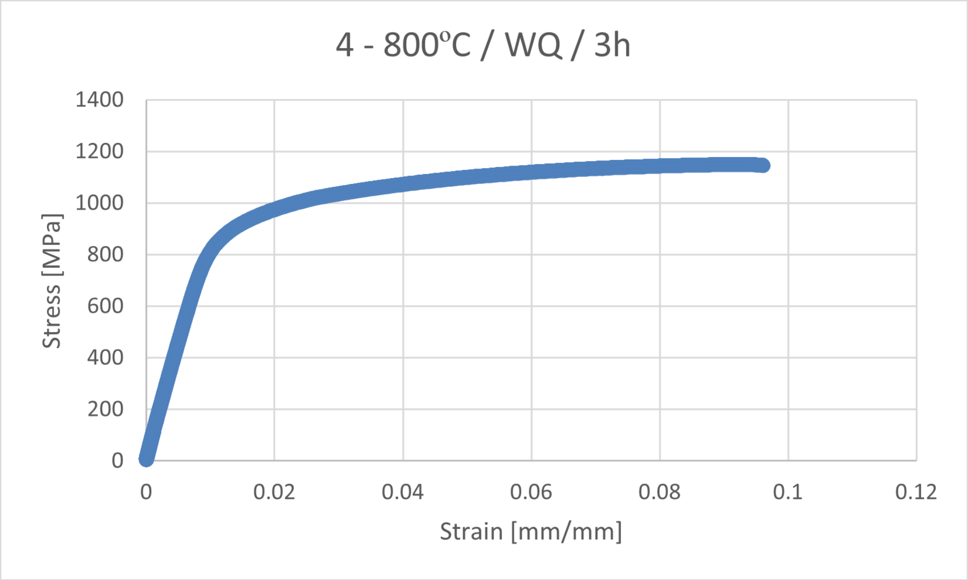

Figure B.5: Stress vs Strain plot for sample number 4.

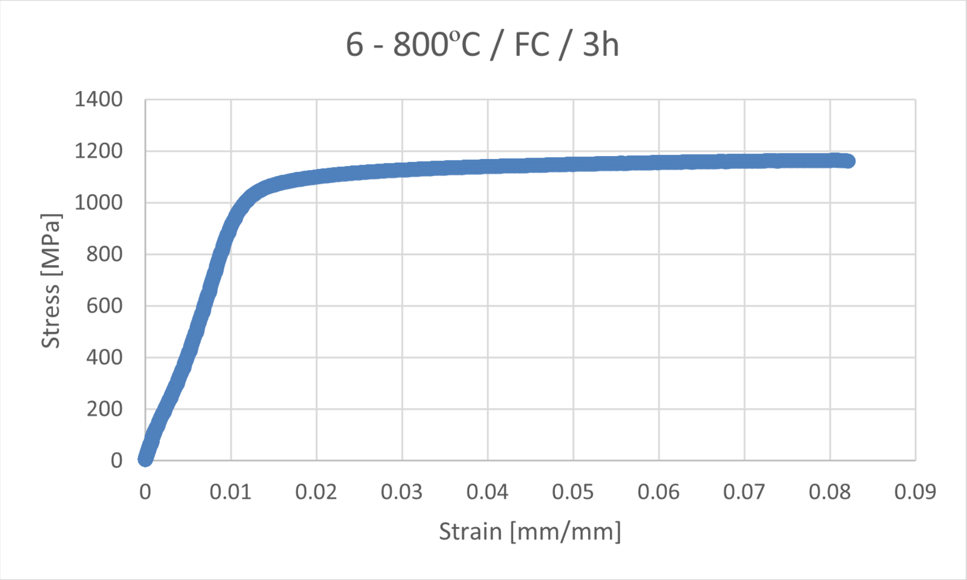

Figure B.6: Stress vs Strain plot for sample number 6.

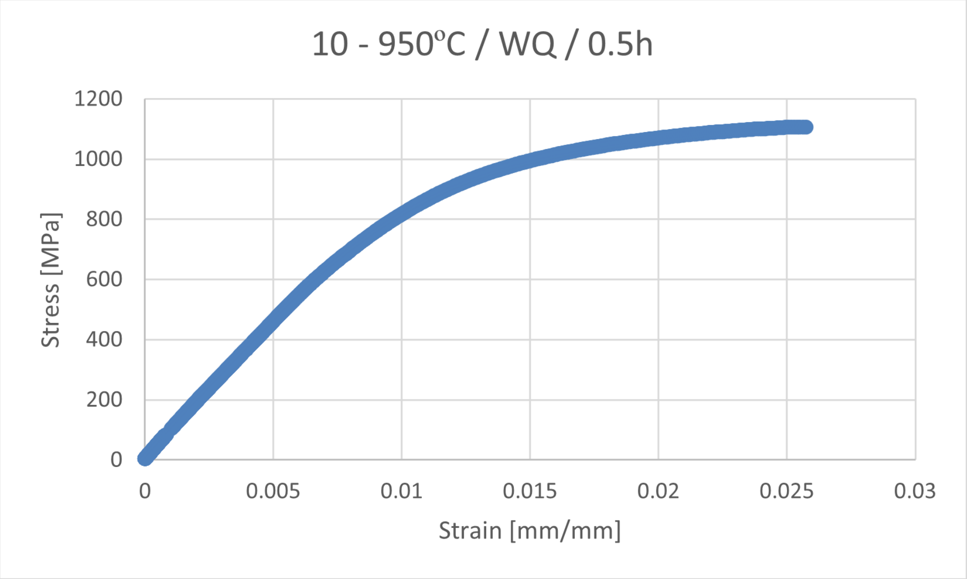

Figure B.7: Stress vs Strain plot for sample number 10.

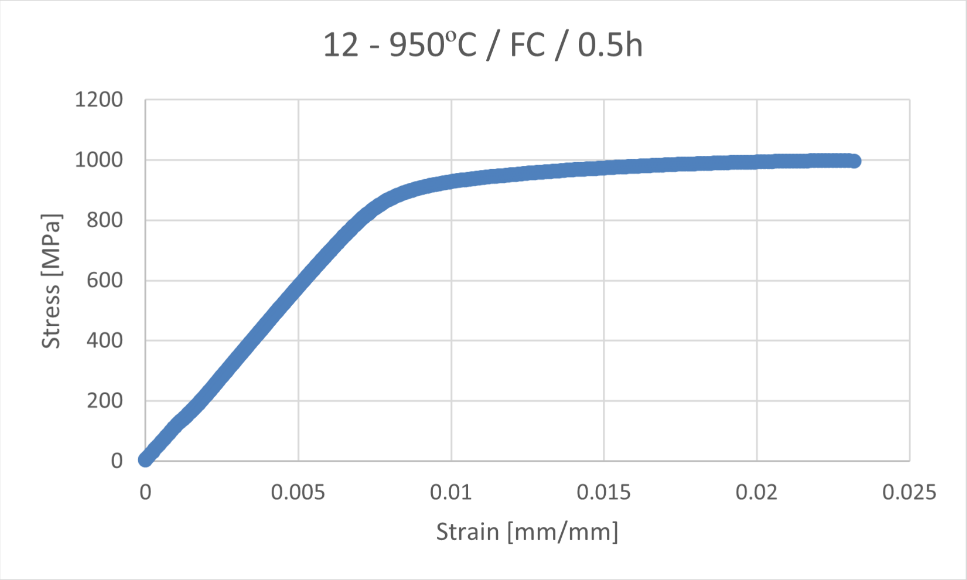

Figure B.8: Stress vs Strain plot for sample number 12.

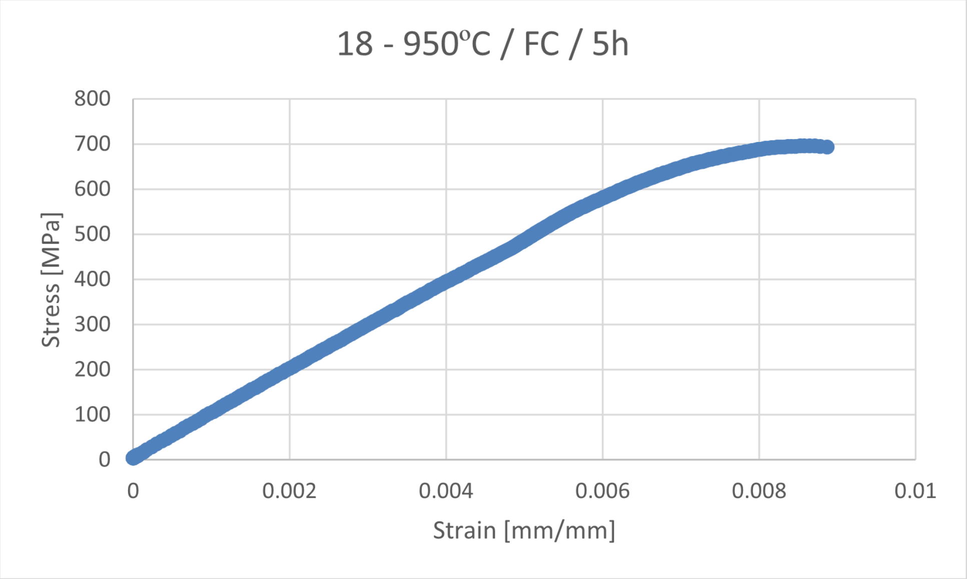

Figure B.9: Stress vs Strain plot for sample number 18.

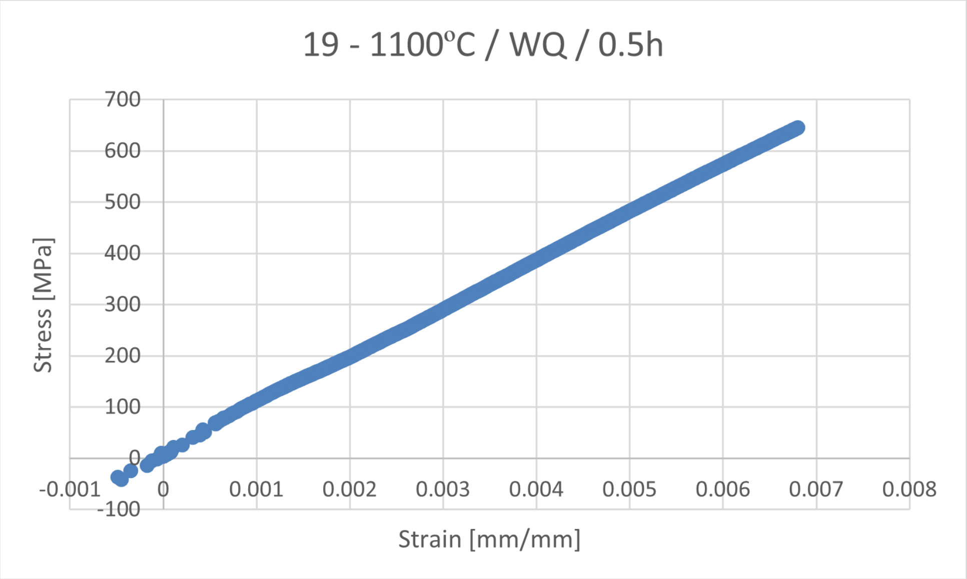

Figure B.10: Stress vs Strain plot for sample number 19.

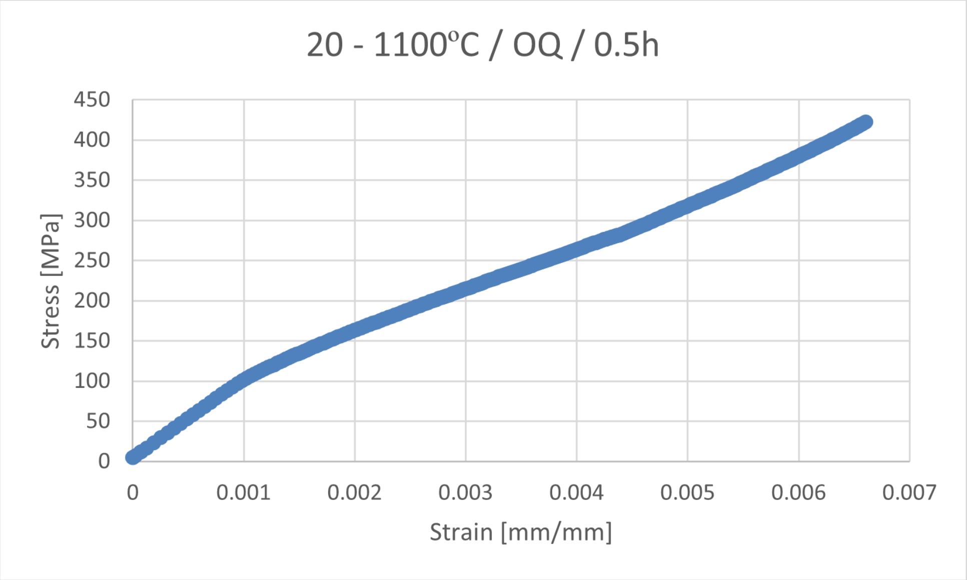

Figure B.11: Stress vs Strain plot for sample number 20.

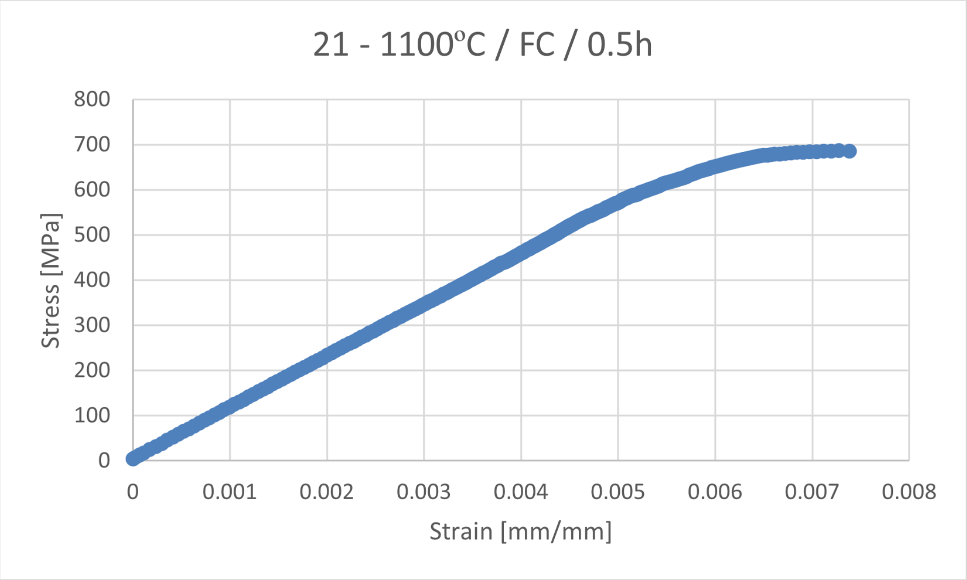

Figure B.12: Stress vs Strain plot for sample number 21.

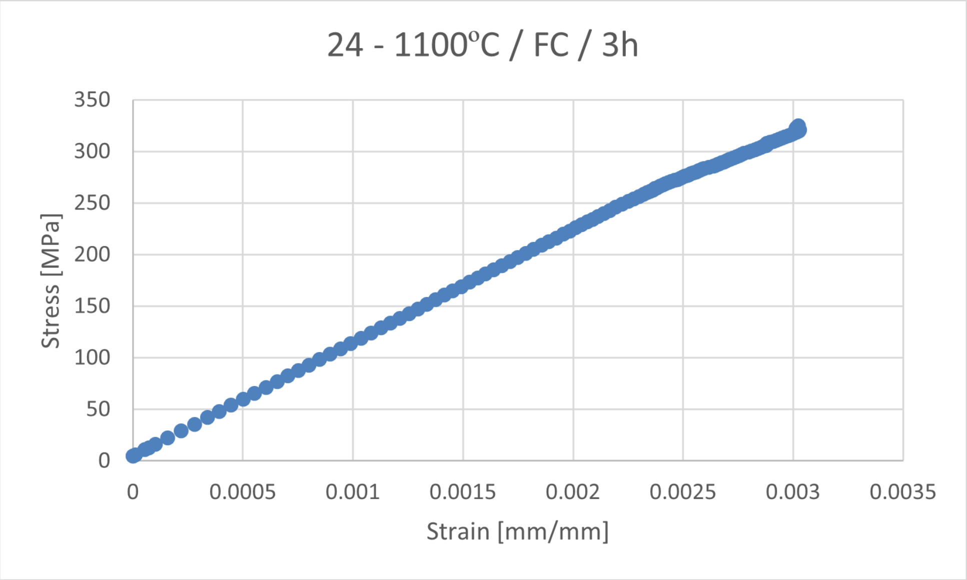

Figure B.13: Stress vs Strain plot for sample number 24.

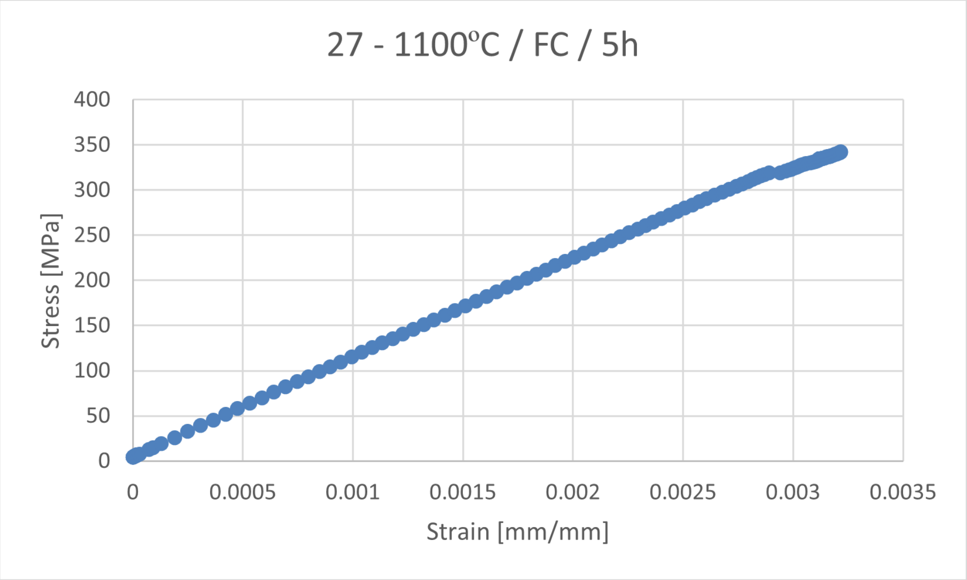

Figure B.14: Stress vs Strain plot for sample number 27.

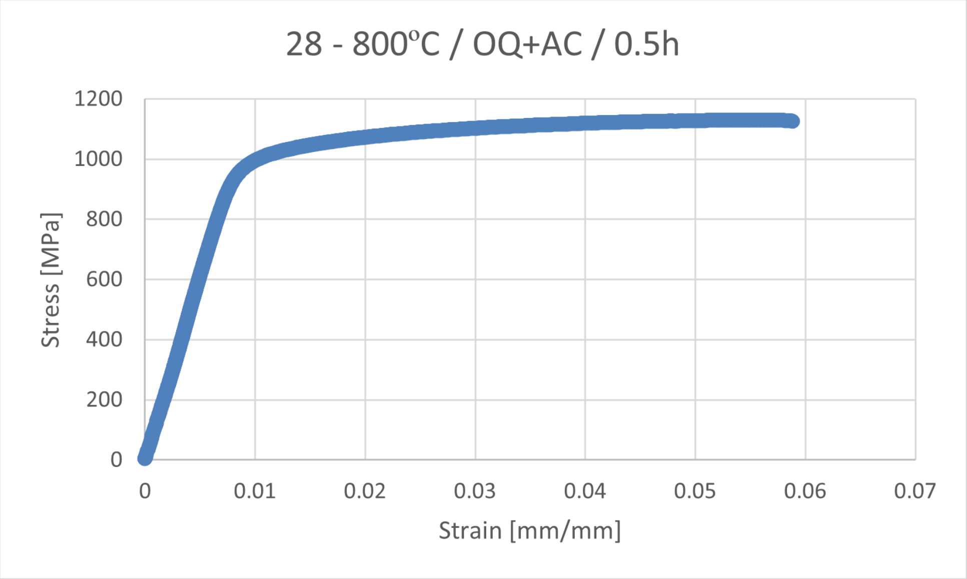

Figure B.15: Stress vs Strain plot for sample number 28.

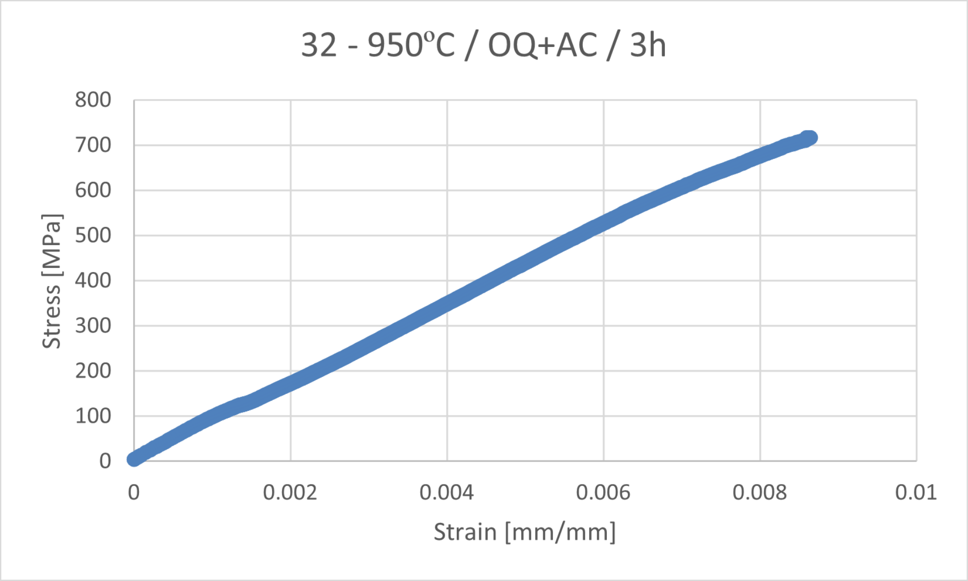

Figure B.16: Stress vs Strain plot for sample number 32.

B.2 Hardness Measurements

Coupon No.	1	2	3	4	5	Average
1	324	422	411	355	342	370.8
2	400	409	401	397	408	403
3	369	386	398	411	393	391.4
4	358	374	360	370	368	366
5	383	400	395	401	380	391.8
6	372	398	330	401	364	373
7	464	473	509	464	410	464
8	354	386	389	375	395	379.8
9	432	430	433	450	467	442.4
10	399	424	397	418	408	409.2
11	507	479	513	503	496	499.6
12	350	371	471	487	399	415.6
13	485	490	531	564	566	527.2
14	516	516	512	501	509	510.8
15	559	557	644	572	558	578
16	506	564	538	487	519	522.8
17	467	482	513	499	538	499.8
18	494	444	517	503	485	488.6
19	508	458	476	488	444	474.8
20	493	495	505	495	506	498.8
21	458	493	443	449	477	464
22	563	581	591	574	606	583
23	599	598	619	620	679	623
24	468	478	478	434	437	459
25	637	561	582	590	536	581.2
26	588	630	588	619	620	609
27	517	482	551	468	457	495
28	361	421	385	388	394	389.8
29	475	433	447	408	407	434
30	425	456	500	457	412	450
31	439	416	425	451	401	426.4
32	414	447	429	469	438	439.4
33	528	577	575	544	504	545.6
34	489	506	507	559	586	529.4
35	625	597	670	616	673	636.2
36	656	661	708	687	645	671.4
P4	430	448	428	451	429	437.2
P5	429	442	429	408	440	429.6

Table B.1: Hardness measurement results, shown in [HV].